EXPERIMENTAL STUDY OF SHOCK WAVE STRENGTHENING BY A POSITIVE DENSITY GRADIENT IN A CRYOGENIC SHOCK TUBE

Thesis by

Viviane Claude Rupert

In Partial Fulfillment of the Requirements
for the Degree of
Doctor of Philosophy

California Institute of Technology
Pasadena, California

(Submitted May 24, 1972)

ACKNOWLEDGMENT

The basic motivation for the work presented here was provided by Dr. H. W. Liepmann whom I want to thank not only for his patient guidance but also for the enthusiasm for their work which he instills in his students.

Drs. A. Roshko's and R. E. Setchell's suggestions and critical review of this thesis are gratefully acknowledged.

I would also like to express my thanks to my parents-in-law, Mr. and Mrs. H. M. Rupert for their assistance in the laboratory and at home.

Mrs. J. Beard's moral support and excellent typing of this thesis deserve my special gratitude.

My appreciation also goes to the National Science Foundation whose financial support allowed me to pursue my studies, as well as to the Sloan Foundation and the Air Force Office of Scientific Research for their support of the experiment.

Finally I want to thank my husband Paul for his help, encouragement and understanding. This work is dedicated to him and our two daughters Emily and Suzanne.

ABSTRACT

An experimental investigation of the strengthening of a shock wave propagating through an isobaric region of increasing density is presented. A new experimental configuration consisting of a pressure-driven shock tube mounted vertically with the test section partially immersed in a cryogenic bath is used. The resulting test gas density distribution consists of a uniform region of low density near the shock tube diaphragm, then a strong local gradient followed by another uniform region of high density. The Mach number of the shock initiated at the diaphragm is determined as the shock emerges from the gradient from velocity and temperature measurements for various initial conditions.

The experimental data are compared with predictions from approximate theoretical models and a numerical integration of the exact flow equations for the shock-gradient interaction. The measured Mach numbers are considerably higher than these predictions indicating that the models are not adequate to represent the experimental configuration. Calculations show that the additional strengthening of the shock results from multiple interactions between waves generated within the gradient and flow nonuniformities due to the shock formation mechanism.

TABLE OF CONTENTS

TABLE OF CONTENTS (cont.)

TABLE OF CONTENTS (cont.)

LIST OF FIGURES

LIST OF FIGURES (cont.)

LIST OF SYMBOLS

a	speed of sound
A, B	calibration constants for resistors
C	symbol used for a compression wave
d	shock tube diameter
$\tilde{D}$	distance between the diaphragm and the density discontinuity (assumed located at average gradient position)
K	calibration constants for resistors
ℓ	test length (distance between the shock and the contact surface)
L	distance between the shock tube support plate and the coolant level
$\tilde{L}$	gradient width
M	shock Mach number
p	pressure
R	resistance in ohms
R_g	gas constant
$\mathcal{R}e$	Reynolds number
S	symbol used for a shock
t	time
T	temperature in degrees Kelvin
u	flow velocity (particle velocity)
U	shock velocity in meters per second
γ	ratio of specific heats
δ	boundary layer thickness
λ	mean free path
μ	viscosity coefficient

LIST OF SYMBOLS (cont.)

ρ	density
τ	test time

Subscripts

1	ahead of the shock
2	behind the incident shock
3	behind the reflected wave
a	ideal (no viscous effects)
cw	determined from the approximate Chisnell-Whitham theory
$i\infty$	for coincident pressure and density discontinuity
m	maximum (due to viscous effects)
max	maximum from numerical computations
mea	measured
o	characteristic parameter in gradient shape function
s	at the shock
∞	for coincident "equivalent" pressure and density discontinuities
F	after merging with first wave reflected on the contact surface
I	incident (on the variable density region)
L	measured from the liquid level
R	reflected from the variable density region
T	transmitted through the variable density region

Superscripts

$\overline{}$	non dimensionalized (ex: $\overline{x}_L = x_D/D$)
$'$	after the variable density region

I. INTRODUCTION

Considerable theoretical and practical interest has been expressed in the strengthening of a shock wave propagating through a nonuniform medium. A number of theoretical investigations (Refs. 1 - 5) and recent experiments at the California Institute of Technology (Refs. 6 and 7) have been conducted to study the strengthening of a shock passing through a convergent channel. Astrophysical problems related to variable stars and novae have prompted theoretical investigations (Refs. 8 - 13) of shock propagating into regions of decreasing density and pressure. The present study is concerned with the experimental study of shock strengthening in regions of increasing density (decreasing temperature) at constant pressure[*], for subsequent use in experiments involving the effect of strong temperature and pressure pulses on cryogenic materials.

The primary objective of the present work was the development of a new shock tube technique for obtaining strong shocks by the novel means of cooling the test gas. Testing of the resulting system provided experimental evidence of shock strengthening by a positive density gradient and disclosed the large additional strengthening effects of reflected waves associated with the shock formation mechanism.

The basic motivation for the development of such a shock

---

[*] Hereafter, an initial "density gradient" is assumed to be a constant pressure region unless otherwise specified.

tube is that the maximum shock strength obtainable in a conventional shock tube depends upon the ratio of sound speed of the driver and test gases. Having chosen the gases, this ratio can be increased by increasing the temperature of the driver gas with respect to that of the test gas. Until the present work this was done experimentally by heating the driver gas. Electrical heating of the driver walls to 1000°K increases the ratio of sound speeds by a factor of 1.82. Constant pressure or volume combustion drivers yield "equivalent speeds of sound" ratio increases of the same order. Very large pressures and temperatures can be obtained using explosive drivers, resulting in extremely high Mach numbers. However, the disadvantage of this method is the loss of part of the apparatus with each test. The rapidly increasing interest in cryogenics, together with the development of low temperature techniques and the availability of cryogenic fluids, suggested the possibility of reversing the usual trend by cooling the test gas rather than heating the driver gas. Using liquid helium as a coolant, an increase in the ratio of sound speeds by a factor of 8.3 can easily be obtained at atmospheric pressure. Higher ratios are available by lowering the vapor pressure of the cryogenic bath. The difficulty of creating a true temperature discontinuity in the laboratory, however, suggested investigating the experimentally more feasible case of a gradient. Here driver and test gases remain at the same temperature across the diaphragm. Downstream of the diaphragm, in the test gas, a temperature gradient followed by a uniform region of low temperature is established. As the shock propagates through the gradient into the low temperature region it is expected to strengthen such that at a large distance downstream from the gradient, it reaches the value corresponding to coincident temperature and pressure discontinuities. The variation in shock strength as the shock propagates through the nonuniform region and within a few gradient widths of the gradient end is assumed to be dominated by the shock-gradient interaction phenomena which have been theoretically investigated.

These theoretical analyses are generally based on the one-dimensional equations of motion for ideal gases. The one dimensional propagation of a shock through a density gradient is similar to shock propagation through a channel with a gradual area change. Experimentally, the intrinsic geometry dependence of the converging channel case creates complex wave patterns (Refs. 6 and 7) which cannot be predicted from the one dimensional equations. However, such effects are not expected in variable density cases studied in a constant area shock tube, provided viscous effects at the walls are negligible. In addition the ideal-gas equations predict a deceleration of the shock in the increasing density case whereas in both the decreasing pressure and convergent channel cases an acceleration is expected. In the last two cases very high enthalpies can be obtained behind the shock (which is the main interest in their study) and eventually ideal-gas equations can no longer describe the flow field and gas properties. For the increasing density case the temperature behind the shock decreases as the shock strength increases; thus, if ideal-gas conditions exist initially, these conditions remain valid throughout the shock motion. The propagation of a shock through a positive density gradient should therefore be correctly predicted by one-dimensional ideal-gas equations. Although a general solution for these nonlinear equations has not been found, an approximate theory for shock motion in nonuniform media has been developed by Chisnell (Ref. 14) and Whitham (Ref. 3). An exact solution of the full equations was also obtained by Bird (Ref. 15) by numerical methods.

The shock strength corresponding to given initial conditions can therefore be calculated. However, an experimental apparatus unavoidably introduces two factors not taken into account by the theory. These are the influences of viscosity due to the existence of confining walls, and the shock formation mechanism which causes the region of uniform flow behind the incident shock to be finite and terminated by a contact surface. Rereflected disturbances on this contact surface can overtake the shock and modify its motion. The probability of this modification occurring within distances of the order of the gradient width is enhanced by the fact that the shock decelerates. Numerical solutions can be extended to include wall effects and the shock formation mechanism, but such computations become quite complex.

Hence experiments were made to insure that shocks of sufficient strength for the projected applications could indeed be obtained with a "reusable" pressure-driven shock tube. The test section of a vertical conventional shock tube was partially immersed in a liquid coolant. The resulting test gas temperature profile was measured. Shock Mach numbers at both the beginning and end of the gradient were computed from measured velocities. Perhaps the most interesting, and certainly the most surprising, result of this study is the unexpectedly high Mach number actually observed. After passage through an extended density gradient located downstream from the shock tube diaphragm, the measured shock Mach number approached the limit of zero width gradient located at the diaphragm. Interpretation of these results in terms of the flow equations and initial and boundary condition is presented.

II. THEORETICAL ANALYSIS

In analyzing the interaction between a shock wave and an isobaric region of increasing density the following assumptions are made:

1. The flow is one dimensional.
2. The gases are thermally and calorically perfect in all regions.
3. The uniform flow behind the incident shock is unbounded.
4. Viscosity and diffusion are neglected and the flow is adiabatic.

However, in a shock tube the uniform region (test length) behind the shock is bounded by a contact surface, and viscosity influences both the shock strength and test length. Modifications to the basic interaction between the shock and the variable density region due to these effects are discussed in the second part of this section.

2.1. Interaction between a Shock Wave and a Variable Density Region

2.1.1 The Discontinuous Density

The simplest density distribution for which an exact solution is possible is the limiting case of a single density discontinuity as illustrated in figure 1a. At some position downstream of an incident shock of Mach number M_I there is a discontinuity in the gas density ρ from conditions 1 to conditions 1' (with the constant pressure constraint $p_1 = p_1'$). The shock jump equations (Appendix A) define state 2 behind the shock. Distances x are measured from the location of the discontinuity and are positive in the direction of the incident shock motion, and time $t = 0$ corresponds to the shock arrival at $x = 0$. Since there is no length scale associated with this problem, the flow properties can only be a function of $x/a_1 t$ (Landau and Lifshitz, Ref. 16) where a is the speed of sound.

Figure 1b shows the flow pattern after the shock has passed the discontinuity. A transmitted shock of Mach number M_T propagates into region 1' while a reflected shock of Mach number M_R propagates back into region 2. Regions 2' and 3, behind the transmitted and reflected shocks respectively, are separated by a transition* surface where density and temperature are discontinuous. This transition surface separates the gas particles which were originally on either side of the density discontinuity. As illustrated in figure 2b the strengths of the transmitted and reflected shocks are determined by matching pressure and velocity across the transition surface. Fluid pressure (p) and velocity (u) behind a shock propagating with a velocity U into a gas at conditions 0 are related by the following equation:

$$\pm (u - u_0) = \frac{a_0}{\gamma_0} \frac{\frac{p}{p_0} - 1}{\left[1 + \frac{\gamma_0 + 1}{2\gamma_0}\left(\frac{p}{p_0} - 1\right)\right]^{\frac{1}{2}}} \qquad p \geq p_0 \qquad (1)$$

---

*"Transition surface" is used here to differentiate this surface from the "contact surface" associated with the initial pressure discontinuity across the shock tube diaphragm.

where γ is the ratio of specific heats at constant pressure and volume, and where the + or - sign apply depending on whether the shock moves in the + or - x direction relative to the fluid, that is on the sign of $(U-u_o)$. The choice of the + x direction implies that the + sign must be used for the incident and transmitted shocks, the - sign for the reflected shock. Conditions 0 correspond respectively to state 1 for the incident shock (curve S_I on the pressure versus velocity diagram of figure 2b), 1' for the transmitted shock (curve S_T) and 2 for the reflected shock (curve S_R). The strength of the incident shock defines conditions 2 on S_I and hence S_R. Since across the transition surface $u'_2 = u_3$ and $p'_2 = p_3$ the intersection of S_T and S_R gives $p'_2 = p_3$ which defines the strength of the transmitted and reflected shocks. Analytically the result is obtained by solving simultaneously the equations corresponding to S_T and S_R. Such computations show that the transmitted shock is stronger but slower than the incident shock $(M_T > M_I$, $U_T < U_I)$.

Since this procedure for determining M_T and M_R was first presented by Paterson (Ref. 17), theoretical predictions for the case of a density discontinuity will generally be referred to as "Paterson's results".

2.1.2 The Continuous Density

The preceding analysis is now extended to the case where the change in density occurs over a finite length $\tilde{L}$ as illustrated on figure 3a. As the shock encounters the increasing density region elements of a compression wave are reflected into region 2 (corresponding to the shock wave reflected in the preceding case as shown in figure 2a). Rather than a single transition surface a transition layer occurs in which density and temperature (and hence entropy) vary continuously. This layer is the "entropy layer" and separates regions 2' and 3 behind the transmitted shock and the reflected compression wave respectively. Neglecting the interaction of this compression wave with the entropy layer, states 2' and 3 are now determined by simultaneously solving the equations corresponding to S_T and C_R (fig. 3b) where the pressure and velocity at each point, of a compression wave C_R are related by

$$u - u_2 = \frac{2\, a_2}{\gamma_2 - 1}\left[1 - \left(\frac{p}{p_2}\right)^{\frac{\gamma_2 - 1}{2\gamma_2}}\right] . \tag{2}$$

The shock strength varies continuously along C_R through the region of increasing density. In the p-u plane C_R lies above the corresponding reflected shock curve (S_R in fig. 3b) so that the strengths of the final transmitted and reflected waves are larger than in Paterson's case. However, sufficiently far from the variable density region ($x/\tilde{L} >> 1$) the gradient appears as a discontinuity, the compression wave coalesces into a shock and Paterson's analysis should apply. The transition in shock strength from values along C_R to its limit value (M_T) as obtained from Paterson's analysis results from the complex wave pattern generated by the interactions of the entropy layer with elements of the initial reflected compression wave. An overshoot of the actual transmitted shock strength compared to M_T could and indeed does occur (Ref. 15) before the asymptotic value is reached.

These phenomena are now considered quantitatively in order to obtain a local relationship between shock position and strength. The flow field is described by the following equations of mass, momentum and energy conservation:

$$\frac{\partial \rho}{\partial t} + \frac{\partial \rho u}{\partial x} = 0 \tag{3}$$

$$\frac{\partial u}{\partial t} + \frac{1}{2}\frac{\partial u^2}{\partial x} = -\frac{1}{\rho}\frac{\partial p}{\partial x} \tag{4}$$

$$\frac{1}{p}\left(\frac{\partial p}{\partial t} + u\frac{\partial p}{\partial x}\right) - \frac{\gamma}{\rho}\left(\frac{\partial \rho}{\partial t} + u\frac{\partial \rho}{\partial x}\right) = 0 \tag{5}$$

The density gradient $\rho/\rho_1 = \bar{\rho}\,(x/\tilde{L})$ extends from $x = 0$ to $x = \tilde{L}$, and $t = 0$ is the time when the incident shock reaches $x = 0$. The boundary conditions are that conditions 2 prevail at $x = -\infty$ and the shock jump conditions (Appendix A) apply along the shock path $x = x_s(t)$. Since the problem now contains a length scale $\tilde{L}$, flow properties are of the form $f\,(x/\tilde{L},\ ta_1/\tilde{L})$. In particular for given M_I , γ and $\bar{\rho}\,(x/\tilde{L})$ the shock strength will be a unique function of $x_s/\tilde{L}$. Similarly p/p_1 , ρ/ρ_1 and u/a_1 (p, ρ and u are measured behind the shock) will be unique functions of $x/\tilde{L}$ and $ta_1/\tilde{L}$.

A general analytic solution of the nonlinear equations (3) through (5) with these boundary conditions has not been obtained. Similarity solutions have been found for certain density distributions, usually for polytropic atmospheres, such as exponential laws (Refs. 8 and 9) and power laws (Ref. 10 and 11). For the isobaric case approximate analytic solutions have been derived for arbitrary density distributions and exact numerical solutions have been obtained for particular spatial density distributions; these analyses and the results which can be derived from them are summarized in the following sections.

Approximate Analytic Solutions

The equations of motion (3-5) can be written in characteristic form:

$$dp + \rho a\, du = 0 \qquad (6)$$

on $dx = (u + a)\, dt$. ("P" characteristic)

$$dp - \rho a\, du = 0 \qquad (7)$$

on $dx = (u - a)\, dt$ ("Q" characteristic)

$$d\,(p\rho^{-\gamma}) = 0 \qquad (8)$$

on $dx = u\, dt$ (particle path)

Behind weak shocks the P characteristics are almost parallel to the shock since $(u + a) \sim U$ when $M \sim 1$.

Hence Whitham (Ref. 3) proposed applying the corresponding characteristic equation (6) to gas conditions just behind the shock. Since these conditions can be related to the known distribution ahead of the shock using the shock jump relations, the result is an ordinary differential equation for $M\,(x_s)$. Whitham suggested that the approximate theory could be extended to higher initial Mach numbers, but he noted that, in general*, there were

---

*The results of similar analyses for shock propagation in convergent channels agreed with corresponding exact solutions.

no formal justifications for such an extension.

The results of the integration of the differential equation for $M(x_s)$ can be written in the closed analytical form:

$$\ln \rho_1 \sim 2 \ln \frac{M_{cw}^2 - 1}{M_{cw}} - 2 \frac{\gamma - 1}{2\gamma} \ln \frac{(z-1)\ (\eta + z)^{\eta}}{(z+1)\ (\eta - z)^{\eta}} \tag{9}$$

where $z^2 = \dfrac{M_{cw}^2 + \dfrac{2}{\gamma - 1}}{M_{cw}^2 - \dfrac{\gamma - 1}{2}}$ and $\eta = \sqrt{\dfrac{2\gamma}{\gamma + 1}}$

For any given initial distribution $\rho_1(x/\tilde{L})$, the Mach number of the shock at a position $x_s/\tilde{L}$ can then be determined by (9). For strong shocks, (9) reduces to $M \sim \rho_1^{\frac{1}{2}-\alpha}$ or $U \sim \rho_1^{-\alpha}$

where $\alpha = \left[2 + \dfrac{2\gamma}{\gamma - 1}\right]^{-1}$.

This result shows that when the shock propagates into a denser fluid it decelerates. However, for all known gases, the decrease in velocity is offset by a more rapid decrease in speed of sound so that the shock Mach number increases. This behavior is qualitatively similar to the discontinuous density case.

Whitham's solution provides no information on the flow field behind the shock. However, Chisnell (Ref. 14) obtained the same result using an approach more amenable to improved approximations. A continuous density gradient is assumed to be equivalent to a succession of weak discontinuities separating regions of constant density (fig. 4a). Paterson's analysis is applied to the initial interaction at each discontinuity. The pressure ratios for such an interaction can be written as:

$$\frac{p_2'}{p_1} = \frac{p_2}{p_1} + d\left(\frac{p_2}{p_1}\right) , \qquad \text{for the transmitted wave} \qquad (10)$$

$$\frac{p_3}{p_2} = \frac{p_2'}{p_2} = 1 + \frac{d\left(\frac{p_2}{p_1}\right)}{\frac{p_2}{p_1}} \qquad \text{for the reflected wave} \qquad (11)$$

where $\rho_1' = \rho_1 + d\rho$ at each discontinuity (12)

Introducing these values in Paterson's equations and linearizing with respect to $d\,(p_2/p_1)$ and $d\rho$ results in an ordinary first order differential equation; the solution of this equation yields equation (9). These results will be referred to as the Chisnell-Whitham (or "CW") results.

The waves reflected at each infinitesimal discontinuity are rereflected on the preceding transition surfaces and eventually overtake the shock. Modification of the shock strength by these rereflected disturbances is neglected in the approximate CW derivation. Consequently this analysis predicts that the local shock strength depends only on the local density value rather than on the past history of the shock motion. As mentioned previously, far from the gradient the succession of infinitesimal steps appear as a single finite discontinuity and the shock strength should asymptotically reach the value given by Paterson's analysis. However, the final Chisnell-Whitham value of shock strength (corresponding to the intersection of S_T and C_R in fig. 3b) remains constant after the shock passes the gradient and is larger than Paterson's value.

To account for this discrepancy Chisnell (Ref. 14) extended his analysis to include effects of the singly and doubly reflected waves (fig. 4b). He first considered the interaction of elements of the reflected compression wave (such as A_2 B_1 in fig. 4b) with the series of transition surfaces (such as A_1 B_1) corresponding to the initial succession of infinitesimal discontinuities. The resulting strength of the reflected compression fan upon emergence from the gradient agrees fairly well (for moderate gradients) with that of the shock reflected from a discontinuity having the same overall density change. Since the reflected waves propagate in the -x direction into a nonuniform region where pressure as well as density decrease, the rereflected waves generated at each transition surface are elements of an expansion wave (Ref. 17). The subsequent interactions of these elements are illustrated in fig. 4b. As a typical element (B_1A_5) of this expansion wave propagates toward the shock, it interacts with particle paths (A_2 B_2, A_3 B_3) and elements of the first reflected wave (A_4 B_3). At each interaction the wave is partially reflected and partially transmitted. Hence, the strength of this doubly reflected wave, and therefore the shock strength upon merging with it, depends on the detailed structure of the flow field behind the shock. Chisnell obtained an integral expression for the strength of the doubly reflected wave at any point behind the shock as a function of shock position but an explicit analytical expression is not available. The interaction of each expansion fan element with the shock (at A_5) will tend to weaken the transmitted shock. The degree of attenuation at the time the shock emerges from the gradient, and the point beyond the gradient at which these secondary interactions are completed depend upon the particular nature of the gradient.

Chisnell computed the final shock strength for a particular initial density distribution and found that the effects of the doubly reflected waves accounted for most of the differences between the CW prediction and the asymptotic Paterson value. He concluded that subsequent multiply reflected waves had little influence on the transmitted shock.

Exact Numerical Solutions

In order to investigate the effects of various parameters on the differences between the approximate CW theory and an exact solution of equations (3-5), Bird (Ref. 15) numerically solved the corresponding characteristic equations (6-8). These equations were integrated between the shock and the particle path originating at the beginning of the density gradient. Upstream of this limiting particle path the flow is a simple wave and the flow variables are defined by their value on the limit path.

Bird's calculations for a positive density gradient show that the Mach number does in fact overshoot its asymptotic (Paterson) value, with the maximum Mach number (M_{max}) occurring at or near the end of the gradient. The maximum value, however, is always lower than the CW solution (as predicted by Chisnell's analysis of doubly reflected waves). For a given density change across the gradient the deviation between M_{max} and M_{cw}

increases as the steepness of the gradient at $x = 0$. Paterson's value is approached more rapidly as the Mach number increases and the ratio of specific heats decreases.

Bird's computations were performed for density distributions which had discontinuous derivatives at one or both of the gradient boundaries. Since such discontinuities are not characteristic of an experimental gradient, similar numerical computations for gradients with uniformly continuous slopes were made in conjunction with the present experimental work*. Figure 5 presents the computed variation in shock Mach number for a gradient defined as follows:

$$\bar{\rho} = \frac{\rho}{\rho_1} = 1 \qquad \bar{x} < 0 \qquad \text{and} \qquad \bar{\rho} = \frac{\rho'_1}{\rho_1} = \bar{\rho}' \qquad \bar{x} > 1$$

$$\bar{\rho} = \left[\left(\frac{1}{\bar{\rho}'} - 1\right)\frac{\bar{x}^2}{\bar{x}_o} + 1\right]^{-1} \qquad 0 < \bar{x} < \bar{x}_o$$

$$\bar{\rho} = \left[\left(\frac{1}{\bar{\rho}'} - 1\right)\frac{(\bar{x} - 1)^2}{\bar{x}_o - 1} + \frac{1}{\bar{\rho}'}\right]^{-1} \qquad \bar{x}_o < \bar{x} < 1$$

where $\bar{x} = x/\tilde{L}$. For a given density change across the gradient $\bar{\rho}'$, the shape of this gradient (in particular its curvature at $\bar{x} = 0$) can be changed by varying the parameter $\bar{x}_o$.

A typical result for $\gamma = 5/3$ obtained from these calculations is shown in figure 5 for an initial Mach number of 2.32 and a density ratio of 68.6. Here M_{max} is within approximately 8% of M_{cw}. A change in the parameter $\bar{x}_o$ from 0.5 to 0.3

---

*Details of these numerical calculations are presented in Appendix B.

which increases the radius of curvature of the density profile near $\bar{x} = 0$ shows that the maximum Mach number decreases. Near the end of the gradient the Mach number displays an almost discontinuous change in slope as described by Bird. The decrease towards Paterson's value is slow, however, primarily due to the smoothness of the gradient at $\bar{x} = 1$.

2.2. Shock Tube with a Variable Density Region in the Test Gas

2.2.1 Effects Due to the Shock Formation Mechanism

Because the shock is expected to decelerate when it encounters an increasing density region, upstream-facing waves generated in this region can have additional effects in an experimental study; not only do they attenuate the transmitted shock after partial reflection from the gradient-induced entropy layer, but these waves can also modify the shock's strength after reflection from flow non-uniformities resulting from the shock formation mechanism. To compare experimental and theoretical results the previously discussed analysis must be modified to include these processes.

The Discontinuous Density

For a first approach to the problem a single density discontinuity is assumed to be located in the test gas at a distance $\tilde{D}$ from the diaphragm position within a shock tube. The diaphragm rupture is assumed to be instantaneous. Figure 6 shows the initial density distribution in the shock tube, and a time sequence of density distributions as the shock propagates down the tube, together with an (x,t) diagram of the various waves for a particular case. $x = 0$ is now taken at the diaphragm location and $t = 0$ corresponds to the diaphragm rupture time. Since the only characteristic length is the distance $\tilde{D}$, the flow variables will be functions of the form:

$$f\ (x/\tilde{D},\ t\, a_1/\tilde{D})$$

As shown in figure 6, the initial wave system involves the formation of a shock wave (OA) in the test gas, a contact surface (OB) separating the gas initially on either side of the diaphragm, and an expansion fan propagating into the driver gas. These are the usual phenomena discussed in shock tube theory (for example Reference 18) and the appropriate equations relating flow variables are summarized in Appendix A. The driver will be assumed sufficiently long so that the reflection of the initial expansion fan on the driver end wall will not affect the flow field during the time of interest.

The interaction of the incident shock with the density discontinuity gives rise to a strengthened transmitted shock (AD), a weak reflected shock (AB) and a transition surface (AC). The reflected shock interacts in turn with the contact surface (OB) resulting in a shock transmitted past the contact surface and a reflected wave (BC) which can be either a shock or an expansion wave. When this wave is a shock, its subsequent interaction with the transition surface will result in a strengthened transmitted shock (CD). The final result is a strengthened transmitted shock (DE) and a weak reflected expansion wave (Ref. 19 and 20).

The strength of the various waves can be obtained in the same manner as for the interaction between a shock and a density discontinuity (section 2.1.1). The uniform gas conditions in the various flow regions are related by the shock jump (Appendix A) and simple wave equations and the conditions that across a contact or transition surface the pressure and velocity are continuous. Calculations were performed for the interactions shown on figure 6. The results show that increasing either the initial Mach number or the density ratio at the discontinuity magnifies the strengthening of the final transmitted shock (DE) and decreases the distance, relative to the discontinuity location, of the point (D) where primary (AD) and secondary (CD) transmitted shocks merge. Moreover for a given driver gas, the strengthening is less for a heavy test gas than for a light test gas since the reflection on the contact surface is weaker.

When driver and test gases are identical the re-reflected wave (BC) will always be a shock and the final transmitted shock (DE) will be stronger than the initially transmitted shock (AD). However, when the gases differ the re-reflected wave (BC) may be an expansion fan, particularly when the initial shock is weak (Ref. 16). The first transmitted shock (AD) will then be overtaken and attenuated by a rarefaction fan (CD). This case will not be discussed further.

It is apparent that additional interactions between the various waves shown in figure 6 will occur. Computations made for certain cases with very large density discontinuities (Part V) show that the strengthening of the transmitted shock due to these secondary interactions can be significant. The physical location of the various interactions depend on the initial gas conditions and incident shock speed, and on the distance between the shock and the contact surface (OB) as the shock encountered the density discontinuity at A. For given driver gas and test gas conditions this distance is proportional to the distance between the density discontinuity and the diaphragm position.

Far downstream $(x/\tilde{D} >> 1)$, after all interactions have occurred, the final strength of the transmitted shock should correspond to the case in which initial pressure and density discontinuities are coincident. For this case the transmitted shock Mach number is simply given by the shock tube equation (Appendix A). Typical Mach numbers obtained from this equation are considerably higher than Paterson's results for which similar discontinuities are infinitely far apart.

The Finite Width Density Gradient

When the test gas contains a finite-width density gradient, the sequence of wave interactions initiated by the diaphragm rupture remains qualitatively similar to that shown on figure 6. The main difference is that the reflected waves generated by the interaction between the incident shock and the gradient form a compression fan, stronger than the corresponding shock in the discontinuous density case (section 2.1.2). Consequently, the re-reflected and re-transmitted shocks (BC, CD) shown on figure 6 are also replaced by stronger compression waves and the interactions are spread over finite regions of the order of the gradient width.

In this case there are two length scales, the gradient width $\tilde{L}$ and the distance $\tilde{D}$ between the diaphragm position and the start of the gradient. However, far downstream $(x/\tilde{D} >> 1$ and $x/\tilde{L} >> 1)$ the final transmitted shock Mach number should again approach the same limiting value corresponding to coincident pressure and density discontinuities. A local Mach number overshoot past this asymptotic value can result from the merging of the (locally stronger) shock transmitted through the gradient with the (locally stronger) compression wave reflected from the contact surface.

2.2.2 Viscous Effects

The magnitude and physical location of the various interactions depend upon the initial shock Mach number and the distance between the initial shock and the contact surface at the time the shock enters the density gradient. In the absence of viscosity this distance or "test length" ℓ increases linearly with shock position relative to the diaphragm location. However, viscosity limits the increase of ℓ due to a deceleration of the shock relative to the contact surface (Ref. 21). A maximum test length and a minimum shock Mach number are reached when the shock and contact surface attain the same speed.

When the boundary layer between the initial shock and the contact surface is laminar, the maximum test length (Ref. 21) has the form

$$\ell_m \sim d^2 p_1 \left[T_1^{\frac{1}{2}} \mu\,(T_1) \right]^{-1} f(M) \qquad (13)$$

where T_1 and $\mu(T_1)$ are the initial test-gas temperature and viscosity respectively, d is the shock tube diameter and f is a function of the Mach number M. For large values of M, $f(M) = 1/M$.

For any arbitrary shock position x_s (measured from the diaphragm location), the test length can be determined from (Ref 21):

$$\frac{1}{2}\,\frac{\rho_1}{\rho_2}\,\frac{x_s}{\ell_m} = -\ln\left[1 - \left(\frac{\ell}{\ell_m}\right)^{\frac{1}{2}}\right] - \left[\frac{\ell}{\ell_m}\right]^{\frac{1}{2}} \qquad (14)$$

The Mach number attenuation due to a laminar boundary layer, at distances from the diaphragm small compared to ℓ_m, (Ref. 22) can be written in the form

$$\frac{M\ (x_s) - M}{M} \sim (d\,p_1)^{-\frac{1}{2}} \left(\frac{x_s}{d}\right)^{\frac{1}{2}} \qquad (15)$$

where M is the initial (nonattenuated) Mach number.

These expressions show that for small diameter tubes and low test gas pressures the Mach number attenuation and test length reduction can become considerable even at short distances from the diaphragm. Conversely, the maximum test length increases with decreasing test gas temperature (since viscosity decreases with decreasing temperature).

When a density gradient exists in the test gas at some distance $\tilde{D}$ from the diaphragm, the shock Mach number at the start of the gradient will be less than the value given by the shock tube equation (Appendix A). Consequently, the Mach number corresponding to coincident initial pressure and density discontinuities will be an upper bound to the limit value for $x/\tilde{L} \gg 1$ and $x/\tilde{D} \gg 1$. A more accurate limit value can be obtained on the basis of an "equivalent" initial pressure ratio across the diaphragm given by the shock tube equation for the actual (attenuated) Mach number. This improved limit will, however, still be an upper bound since viscous attenuation of the transmitted shock beyond the density gradient will also occur. Similarly, the Mach number of the transmitted shock, as it propagates down the tube and interacts with various waves (section 2.2.1), cannot be determined from the ideal flow pattern corresponding to the initial conditions before diaphragm rupture. The strength of the various waves are determined more accurately based on an initial shock strength corresponding to the "equivalent" pressure ratio. An improved approximation to the location of the interactions can then be obtained by scaling distances measured from the start of the gradient by the ratio of actual to ideal (equivalent) test length as the shock enters the gradient. As the shock propagates into a denser (colder) medium viscous effects become less important as the viscous scaling length ℓ_m (eq. 13) increases.

III. EXPERIMENTAL APPARATUS AND OPERATING CONDITIONS

This section presents a brief description of the experimental apparatus including the shock tube proper, the cryogenic system and the gauges used to measure the shock velocity and the initial temperature distribution in the test section (details will be found in Appendix C). The choice of the operating conditions and the room temperature performance of the system are also discussed.

3.1 Shock Tube Description

To obtain a shock wave incident on a positive density gradient, a pressure driven shock tube was mounted vertically such that the test section was partially immersed in a cryogenic bath. As shown on figures 7a and b, the shock tube proper is comprised of three parts: the room temperature (low density) and cooled (high density) portions of the test section, and the driver section. A large plate was welded onto the test section to support the shock tube in the cryogenic container (fig. 7c). The upper surface of this plate is used as the reference $(x = 0)$ station for all measurement made along the shock tube axis (x is taken as positive towards the cooled part of the test section). Dimensions were limited by dewar sizes and available laboratory space. This resulted in the choice of a 1.5 in. i.d. cylindrical tube with an overall test section length of 96 in. and driver length of 10 in. Specific design details and dimensions are summarized in Appendix C.

The choice of suitable materials was dictated by heat flow patterns and by the constraints imposed by the cryogenic environment. In order to minimize the vertical heat flow from the liquid coolant to the room temperature section, stainless steel tubing with low thermal conductivity was used for the lower portion of the test section. The tube walls were chosen as thin as practical to insure both minimum vertical heat flow and maximum lateral conduction (to rapidly cool the test gas between runs). The upper part of the shock tube was made of higher thermal conductivity steel and brass. A 1.5 in. ball valve was an integral part of the test section to avoid condensation when the shock tube was opened to change diaphragms. To provide a seal between the bottom of the shock tube and the end plate (velocity gauge support) which would remain vacuum tight at liquid helium temperatures, indium solder was forced to cold flow in a thin circular groove machined in the end plate.

The vertical geometry was a determining factor in the choice of diaphragm material and bursting pressure, since diaphragm fragments fall down the tube damaging the gauges mounted on the end wall. Soft aluminum .003 in. thick and properly positioned knife blades (Ref. 23) gave both a repeatable driver pressure and clean diaphragm cuts.

Contaminants in the test gas were minimized by passing the gas through a liquid nitrogen trap before entering the shock tube.

Pressure in the tube on either side of the ball valve was measured with a 10 mm Hg absolute pressure gauge (Barocel) and a 20 mm Hg gauge (Hastings). The driver pressure was monitored with a manometer (Kollsman manifold pressure gauge).

3.2 Shock Velocity Measurements

In order to determine the strengthening of the shock due to the density gradient, the shock Mach number has to be measured before and after the nonuniform region. Hence both the velocity of the shock and the speed of sound (or temperature) of the test gas have to be measured for each region of the test section.

3.2.1 Upper (Side Wall) Gauges

The velocity of the initial shock incident on the gradient was measured with conventional thin-film gauges mounted in the shock tube walls just below the ball valve (fig. 7a and 7c). Their signals were amplified and fed to an elapsed time counter. The distance between the gauges was accurately measured (100.54 ± .30mm) and shock velocities were directly computed from the elapsed times. The accuracy of the velocity measurements was limited by the use of a one megacycle counter with a nominal accuracy of ± 1 digit (LSB). As a result errors as large as 2.4% could have occurred within the range of measurements. However, comparison of counter data with data obtained from oscillograms indicated that, in the average, the counter data were within 1% of their true value. An additional error of less than .25% also resulted from the slight difference in signal shape for the two gauge elements used. The final accuracy of the velocity measurements was 1.3% RMS.

3.2.2 Lower Gauges

The two types of gauges used for measuring shock velocities in the high density region are shown in figure 8. The "filament" gauge consisted of platinum coated pyrex filaments epoxied to thin glass needles (Ref. 24). The supporting needles were mounted on the shock tube end wall. Each filament was independently connected to a measuring circuit through a vacuum tight multipin connector mounted in the tube end wall. The results obtained with this gauge were excellent but a breakage problem led to the use of an alternate "slide" gauge. The slide gauge consisted of two thin platinum films baked on the flat side of a glass slide, the leading edge of which was wedge-shaped to minimize flow disturbances. The slide was again mounted to the shock tube end wall and electrical contact to the platinum films was obtained as in the case of the filaments. For both types of gauges, the shock velocity was measured by timing the shock passage between two filaments or thin films. The distance between gauge elements was measured prior to fastening the end wall to the test section. The responses of two gauge elements were differenced and recorded on oscillograms. The time interval between the shock's arrival at the elements positions was read on the oscillograms. Errors in the resulting velocity were due to the errors in the distance between gauge elements and timing errors. Distances were measured with a Kodak optical comparator resulting in a .1% RMS error. Timing errors were due to uncertainties in locating the exact beginning of each signal on the oscillogram and in the oscilloscopes time bases. A calibrated pulse generator was used as standard to determine the oscilloscopes sweep rates and since, by differencing the gauge elements signals a single trace needed to be read, synchronization errors were avoided. The final accuracy of the velocity measurement was 2% RMS.

Typical gauge responses are shown on figure 9. The main difference between the two types of gauges was their response to heat transfer after the shock passage (Ref. 24). However, measuring the time interval between signals from separate gauge elements was equally accurate.

3.3 Cryogenic System

The cryogenic system configuration depended on the liquid coolant used. When liquid nitrogen was used only a "LN_2[*] dewar" was installed (fig. 7a). This dewar was a commercial stainless steel dewar $8\frac{1}{4}$ in. i.d. and 32 in. long. An additional insulated collar (fig. 7a) was added to obtain a total inside length of 38.5 in. It was open to the atmosphere 5.5 in. below the shock tube support plate so that 35 in. of the test section were located within the dewar. The maximum boil off rate of the liquid nitrogen was less than 1.5 in./hr. in all operating conditions.

An additional "LHe dewar" was installed within the LN_2 dewar when liquid helium was used as a coolant. The LHe dewar was a glass dewar 6 in. i.d. and 44.5 in. long. The top 9 in. was a solid walled section, used for supporting and vacuum sealing the dewar, so that 30 in. of the shock tube section were located in the usable part of the LHe dewar. The maximum boil off rate of the liquid helium in operating conditions was 2 in./hr.

The liquid level in both dewars was measured with a "dipstick" consisting of a narrow strip of balsa wood attached to a styrofoam float (Ref. 25).

---

[*] "LN_2" and "LHe" refer to liquid nitrogen and liquid helium respectively.

3.4 Gradient Measurements

Rather than installing additional gauges to measure the temperature in the shock tube prior to each run, a removable "resistor ladder" was used to determine the temperature distribution as a function of liquid coolant level during separate gradient measurement tests. Apart from slight changes due to the temperature probe, the gradient depends only on the coolant level, provided atmospheric pressure (which controls the coolant temperature in these tests) and temperature are constant.

Temperature was obtained from the measured resistance of 1/8 watt Allen Bradley resistors which have a temperature variation of the form (Ref. 26 and 27)

$$\log R + \frac{K}{\log R} = \frac{A}{T} + B$$

where K, A and B are calibration constants. Details of the resistors calibration and resistor ladder characteristics can be found in Appendix C.

During the gradient measurement tests a number of these resistors were mounted at fixed positions on a balsa wood frame which rested on the test section end wall. Variations of the temperature profile in the shock tube, due to the insertion of the probe, were minimal and the gradient can be determined to within 2%.

3.4.1 Temperature gradient Using Liquid Nitrogen as Coolant

The gradients were measured with eight resistors positioned along the shock tube axis. The data from these measurements were plotted for various liquid levels L , measured from the shock tube support plate, on figure 10. The separate data points shown for two of the liquid levels correspond to different relative positions of the resistors. As expected the temperature reached its maximum value (ambient temperature) close to the location of the support plate. The minimum value (coolant temperature) was reached close to the liquid level and as the level decreased the gradient stretched accordingly. The collected data from the measurements were plotted on figure 11 as a function of a normalized distance $\bar{x} = x/L$. On figure 11 each symbol corresponds to a different liquid level; the solid curves correspond to the minimum and maximum liquid levels for which data were obtained. The shape of the temperature profile does not vary significantly as a function of $\bar{x}$ although a slight shift in origin would be required to obtain a single profile.

3.4.2 Temperature Gradient Using Liquid Helium as Coolant

In this case twelve resistors were used. The first three resistors were located above the shock tube support plate to verify that the upper section remained at room temperature.

The data were plotted for various liquid levels on figure 12. As in the LN_2 case the gas reached room temperature close to the support plate. The gradient was extremely steep between this location and the top of double walled portion of the helium dewar ($x = 9$ in). In this interval the temperature decreased to approximately liquid nitrogen temperature*. Beyond this point the temperature decreased to the coolant temperature a short distance below the liquid level.

Collected data from these measurements were plotted versus $\bar{x}$ in figure 13. Again the temperature distribution scales reasonably well with the coolant level L .

---

*The liquid level in the outside LN_2 dewar was maintained within an inch above the start of the LHe dewar double wall.

3.5 Operating Conditions

3.5.1 Initial Conditions

The lowest possible temperatures in the test gas are obtained using liquid helium as coolant. This restricts the choice of the test gas to helium. For less severe cooling conditions other test gases could be used. In order to obtain data for a heavier diatomic gas, nitrogen was chosen for use at LN_2 temperatures.

Since a high initial Mach number was desirable a light gas was required for the driver gas. Helium was chosen as it is less hazardous than hydrogen. The driver pressure was approximately 95 psia for all runs.

The choice of the initial test-gas pressure was dictated by a compromise between a number of factors:

a) The pressure had to be significantly less than the vapor pressure of the test gas at the coolant temperature in order for the gas to be considered perfect*.

b) With a fixed driver pressure, a low test gas pressure is required to obtain a high incident shock Mach number. The ratio of limiting boundary layer thickness to shock tube diameter also decreases with increasing Mach number (Ref. 21). However, the usable test length scales with the maximum test length (l_m) which is proportional to the initial pressure and inversely proportional to the shock Mach number (section 2.2.2). Also, the Mach number

---

*At 4°K the correction to the compressibility factor for helium is approximately .1% at 3 torr pressure (Ref. 28). The influence of pressure on speed of sound required for Mach number calculations can be found in Ref. 29.

attenuation at a fixed distance from the diaphragm decreases as p_1 increases. A compromise is therefore required between high initial Mach numbers (low initial pressure) and long test times with minimum Mach numbers attenuation (high initial pressure).

c) The ratio of the mean free path (λ) to the shock tube diameter (d) must remain small in order to insure continuum conditions through the flow. Pressure on the order of .4 torr for helium and .14 torr for nitrogen is required for λ/d values less than 1% (at ambient temperature).

For runs using helium as a test gas, a pressure of 2 torr was chosen as a reasonable balance of these considerations. Nitrogen runs were made at initial pressures of 2 torr and .8 torr. The corresponding values of λ/d at room temperature were respectively 3×10^{-3}, 7×10^{-4} and 1.7×10^{-3}.

3.5.2 Room Temperature Performance

The Mach numbers measured at the upper side wall gauges locations were lower than corresponding values computed from the ideal shock tube equation with the given pressure ratios. These differences are primarly due to viscous attenuation*. The attenuation for the shocks in nitrogen is consistent with the value computed from the graphical data presented by Mirels (Ref. 22). A similar comparison is not available for the helium case although in all

---

*Nonideal Mach numbers could result from the influence of the diaphragm opening mechanism (Ref. 30); however any perturbation in the flow field behind the shock due to this process should be minimal at the location of the gauges (more than 20 shock tube diameters from the diaphragm).

cases the measured Mach number is higher than the limit value corresponding to the contact surface speed (Ref. 21).

To estimate the effects of the boundary layer on the flow field behind the incident shock, the maximum test time τ_m*, maximum test length l_m and Reynolds number $\mathcal{R}e_m$ based on l_m were calculated using Mirel's formulas (Ref. 31 and 32). Both laminar and turbulent boundary layers were considered. From these results (and the experimental values reported by Roshko and Smith, Ref. 33) it was concluded that the boundary layers behind the incident shocks, in all experimental conditions, were laminar. Signals from the side wall gauges were indeed characteristic of laminar boundary layers. The computations also showed that, when the shock arrived at the upper gauges, the test length had reached 70% of its asymptotic value for the 2 torr helium case and only 21% of this value for the 2 torr nitrogen case. Thus, in the nitrogen case the flow field behind the shock was unsteady when the shock reached the temperature gradient. In the helium case the flow field was nearly steady.

Table I summarizes the laminar boundary layer parameters for the experimental conditions prior to the gradient.

---

*Maximum time between passage of the shock wave and the contact surface at a fixed location.

TABLE I

Test gas	He	N_2	N_2
p_1 torr	2.	2.	.8
M_I (ideal)	2.83	5.47	6.12
M_{mea} upper gauges	2.36	5.13	5.74
ℓ_m cm	22.4	46.	18.
τ_m μs	137.	320.	107.
Re_m	2.1×10^4	1.6×10^6	9.1×10^5
$\ell/\ell_m = \tau/\tau_m$ at upper gauge	.7	.21	.53
$\frac{\delta_m}{d}$ *	.06	.01	.008

*δ_m is the limit boundary layer thickness (Ref. 21)

3.5.3 Note on Experiment Design

The difficulty in separating experimentally the interaction between a shock and a density gradient from the influence of waves reflected on the contact surface is emphasized by the data presented in Table I. The strengthening of the first transmitted shock by waves reflected on the contact surface occurs at a distance from the density gradient on the order of the test length (Part V). To study the gradient effects alone the gradient width would have to be at least an order of magnitude smaller than the local test length. This could be done by either creating a very narrow gradient (less than a tube diameter in width) or by increasing the test length at the gradient location. Since $\ell_m \sim p_1 d^2/M$ (section 2.3), increasing the test length involves either decreasing the initial shock strength (decreasing the driver pressure), increasing the initial pressure, or increasing the tube diameter. Maintaining a high incident Mach number requires increasing simultaneously test and driver gas pressures, or increasing the tube diameter. The test gas vapour pressure at the coolant temperature bounds the possible increase in pressure. In addition to difficulties in maintaining a constant temperature over the cross section of the tube, a prohibitive use of coolant, especially for liquid helium, would result from sufficiently increasing the tube diameter. Decreasing the gradient width would also result in large coolant losses by thermal conduction along the tube walls, and would require the development of new gauges capable of measuring shock velocities over distances an order of magnitude smaller than the tube diameter.

IV. EXPERIMENTAL RESULTS

Shock velocities were measured at a fixed position in the high density region of the shock tube while the coolant level varied. Shock strengthening, resulting from passage through the gradient, could thus be determined. The effect of varying the test gas, the initial Mach number and the overall density change were observed. The data were compared with the exact numerical solutions and approximate theoretical results for an unbounded uniform flow behind the incident shock, and with the asymptotic values corresponding to coincident pressure and density discontinuities.

4.1 Liquid Nitrogen Coolant

The liquid nitrogen coolant produced an overall density change of $\rho_1'/\rho_1 = 3.88$. Several measurements were made for each of the initial conditions listed in Table I (section 3.5.2) with the liquid level maintained at a fixed location. The measurements were repeated for a number of coolant levels so that the shock strength was obtained at positions x (from the shock tube support plate) varying from L to $2.4 L$, where L is the distance between the liquid level and the shock tube support plate. The data are plotted on figure 14 as a function of distance from the coolant level $(x_L = x - L)$*; each datum point represents an average of the measurements made for a given incident shock and liquid level and the bars indicate the RMS deviation of these measurements. For each incident shock the velocity has decreased

---

*Since the measured velocity was an average over the position of the two gauge elements used, the corresponding value of x was chosen as the average of the two elements' locations.

from its initial value (U measured before the gradient), yet appears to increase with distance from the nonuniform region*.

Since the speed of sound, at the location of the shock velocity gauge, was known from the temperature distribution (for all liquid levels used it was simply the coolant temperature), shock Mach numbers were computed from the velocity data. Figures 15 and 16 show the Mach numbers plotted with respect to $\bar{x}_L = (x/L - 1)$. As expected, the Mach number of the shock after it has traversed the gradient is considerably higher than the Mach number of the incoming shock. The acceleration evident in the velocity data (fig. 14) is emphasized by normalizing distances with L.

Figures 15 and 16 also show results from theoretical calculations corresponding to the same initial Mach numbers and density distribution but for the idealized case of an unbounded uniform flow behind the shock. Beyond the gradient the CW approximate analysis gives a constant Mach number M_{cw} which represents an upper bound (depending only on the overall density change and not on the density distribution within the gradient). The exact numerical computations (Appendix B) were performed for a typical measured temperature profile $T/T_1 = \bar{T}(x/L)$. Since all measured temperature profiles are similar when plotted versus x/L (fig. 11 and section 3.4.1) and only a shift in origin is needed to obtain a single profile, the similarity solution indicated in section 2.1.2

---

* Data taken on a few occasions at different x's, for the same incident Mach numbers and liquid level, also indicated a slight acceleration of the shock beyond the gradient.

shows that the same shift in $\bar{x}_L$ will give the exact (numerical) solution $M(\bar{x}_L)$ for all liquid levels for a fixed M and γ; only one such curve is shown on figures 15 and 16.

The disagreement between the experimental results and these theoretical predictions is quite evident. Not only are the measured Mach numbers higher than the limiting CW value, but the experiments indicate a definite acceleration of the shock in a region where a deceleration is predicted by the theoretical analysis. However the measured Mach numbers are lower than the asymptotic value $M_{i\infty}$ corresponding to coincident pressure and density discontinuity (section 2.2.1).

4.2 Liquid Helium Coolant

Liquid nitrogen can easily be transferred without undue losses, but liquid helium transfer must be accomplished through rather cumbersome double walled tubes. Frequent transfers are inefficient and expensive since each requires considerable cooling of part of the equipment and is therefore accompanied by a large loss of coolant.

Consequently, rather than maintaining the liquid at a fixed level in order to obtain a statistical sample of velocity data for that level (as in the liquid nitrogen case), the coolant level was allowed to decrease continuously as a result of evaporation. The rate at which data were obtained was only limited by the requirement for steady initial conditions prior to each test. As many as 60 runs were made for a single dewar fill.

In order to examine the behavior of the shock velocity within the gradient some measurements were made when the gauges were close to (or slightly above) the liquid level. In these cases the speed of sound was calculated on the basis of the temperature measured at that location during the gradient measurements.

The overall density change here is $\rho'_1/\rho_1 = 68.6$. The measured velocities are shown on figure 17 as a function of position below the coolant level. As in the liquid nitrogen tests, the velocity has decreased considerably. The minimum velocity is 1030 m/s in comparison to 1790 m/s observed for the same initial conditions except for liquid nitrogen as coolant. An increase in velocity with distance from the nonuniform region is again evident.

Figure 18 shows shock Mach numbers computed from the velocity data and the measured temperature distributions. A maximum value of 9.03 was measured, whereas for a conventional pressure-driven shock tube at room temperature the maximum Mach number attainable predicted by the shock tube equation is 4.29 (helium into helium).

The prediction of the CW theory and the results of numerical computations for a typical gradient are also shown in figure 18. As in the case of the liquid nitrogen coolant, the measured Mach numbers greatly exceed these idealized theoretical results but are lower than the asymptotic value $M_{i\infty}$.

4.3 Summary

The experimental data are summarized in Table II.

Table II

Experimental Results

Gas/Coolant	He/LHe	He/LN_2	N2/LN_2	N2/LN_2
ρ'_1/ρ_1	68.6	3.88	3.88	3.88
M_{mea}	2.36	2.36	5.13	5.74
M'_{mea} *	7.94	3.63	7.43	8.53
M'_{mea} **	9.03	4.07	7.82	9.11
% average increase in measurement range	260	61	48	55

M_{mea} and M'_{mea} are measured Mach number before and after the gradient respectively

*measured at the minimum distance from the gradient

**measured at the maximum distance from the gradient

These results show that an increase in the overall density variation or the initial shock Mach number enhances the strengthening of the shock. For the same overall density change the observed shock strengthening for helium as a test gas is considerably larger than when nitrogen is used in the test section, even though the initial Mach number is lower for helium than for nitrogen.

In addition to the shock strengthening information provided by these tests, qualitative data were obtained on available test times. Oscillograms of the lower velocity gauge signals showed that at the gauge's location the test time was limited by the arrival of the shock reflected from the end wall. Test times of at least 50 μs (liquid nitrogen coolant) and 80 μs (liquid helium coolant) were observed.

V ANALYSIS AND DISCUSSION OF THE EXPERIMENTAL DATA

The experimental data presented in Part IV indicate that shock formation and viscosity effects have to be considered in analyzing the interaction to the shocks with the density gradients.

The characteristic lengths associated with these phenomena are presented in Table III.

TABLE III

All lengths in centimeters

$M_{mea.}$	2.36	5.13	5.74
Test gas	both helium cases	N_2	N_2
L support plate to coolant level	41 to 98	41 to 94	41 to 94
$\tilde{D}$ distance diaphragm-gradient midpoint	133 to 161	133 to 159	133 to 159
l_a ideal test length at $\tilde{D}$*	51 to 62	26 to 31	25 to 31
l_m maximum test length*	22.4	46	18
Average bottom gauge position from support plate	98	98	98

*Room temperature was assumed in computing the values ℓ_a and ℓ_m

A computation of the Reynolds number, assuming the flow was entirely at LHe temperature, suggested that the boundary layer behind the shock would be turbulent. However, it is not clear whether the value of the critical Reynolds number used at room temperature (Ref. 31), would still be valid criterion at low temperatures. Side wall gauge signals obtained when LHe was used as coolant displayed no significant features until the expected time of the contact surface arrival at the gauge location. Hence the boundary layer seemed to have remained laminar, and the value of ℓ_m in Table III is based on Mirel's laminar boundary layer analysis (Ref. 31).

In terms of the "gradient" width L, measurements have been made in the range $0 \leq \overline{x}_L < 1.4$, where $\overline{x}_L = (x/L-1)$. In the absence of shock formation or viscosity effects (section 2.1), a uniform decrease in Mach number from some peak value, smaller than the Chisnell-Whitham prediction to Paterson's limit value should have been seen (section 2.1.2). From numerical computations the total deceleration should be less than 3% for the nitrogen cases and either 5% or 39% for the helium cases using LN_2 or LHe respectively. A typical result of such computation is shown in figure 19. At the location of the shock velocity gauge the Mach number should have decreased less than 2% from the peak value in the nitrogen cases and less than 3% or 9% respectively for the helium cases.

5.1 Contact Surface Effects

A simplified analysis of the contact surface effects is possible by replacing the gradient by a discontinuity having the same overall density change and placed at the actual gradient midpoint. Computations relative to the first set of interactions resulting from waves reflected at the contact surface (as described in section 2.2.1) are summarized in Table IV and figure 20. Distances are measured from the diaphragm location.

TABLE IV

Driven gas/Coolant	He/LHe	He/LN$_2$	N$_2$/LN$_2$	N$_2$/LN$_2$
M_{mea}	2.36	2.36	5.13	5.74
ρ'_1/ρ_1	68.6	3.88	3.88	3.88
M_T *	3.92	2.94	7.05	7.94
M_F **	5.56	3.36	7.78	9.02
$(M_F-M_T)/M_F$ %	34.5	13.0	9.7	12.8
$x_D/\tilde{D}$ +	1.18	1.98	1.58	1.55
$(x_D-\tilde{D})/\ell_a$+	.47	2.54	2.91	2.87

*Shock Mach number after initial interaction with the density discontinuing

**Shock Mach number after merging with the first reflected shock from the contact surface

+Relative location of the merging point

The measurements were made in the range $1.3 < x/\tilde{D} < 1.6$. For the nitrogen cases the strengthening of the first transmitted shock (at D on figure 20) occurs within this range. For the helium cases this strengthening occurs prior to the range of shock velocity measurements when liquid helium is the coolant, and beyond it when liquid nitrogen is used.

Because relatively strong compression waves rather than shocks are reflected in the case of a finite width gradient (section 2.2.1) local Mach numbers larger than those presented in Table IV should be observed in the experiments. The strengthening of the initial shock by the compression fan reflected at the contact surface, and by further reflected waves, thus offsets the weakening effect of the expansion wave originating within the gradient itself. The relative scale of these effects results in a net acceleration of the shock beyond the gradient as was experimentally observed.

5.2 Viscous Effects

In the absence of viscous effects the shock Mach number "far from the gradient" ($x/L >> 1$, $x/\tilde{D} >> 1$) has an upper bound equal to the Mach number ($M_{i\infty}$) predicted for coincident pressure and density discontinuities at the diaphragm location. However, the shock is actually attenuated as it propagates along the tube. Hence the measured Mach number at the gradient entrance (M_{mea}) is less than predicted by the ideal shock tube equation for the given pressure ratio. An "equivalent" pressure ratio (section 2.2.2) corresponds to the measured value M_{mea}. More accurate comparisons between experimental and computed data result from using this equivalent pressure ratio for all computations as was done for the data presented in Table IV. A more accurate limit value (M_{∞}) to the shock Mach number is also given by assuming the equivalent pressure change and the density discontinuity are coincident at the gradient midpoint. Alternately the attenuation, at the gauge location, of a shock with initial Mach number $M_{i\infty}$ can be computed from Mirel's data (Ref. 22), at least for the nitrogen cases. The maximum attenuation of such a shock can also be computed (Ref. 21). Table V presents the values of $M_{i\infty}$ and the corresponding attenuated Mach numbers, together with the values for M_{∞}. Since in computing M_{∞} the discontinuities are assumed to be located at the gradient midpoint, no additional attenuation need be considered in the measurement range.

The values for M_{∞} are presently the best available estimate of limiting Mach numbers in the presence of viscous effects.

TABLE V

Driver Gas/Coolant	He/LHe	He/LN_2	N_2/LN_2	N_2/LN_2
M_{mea}	2.36	2.36	5.13	5.74
$M_{i\infty}$	11.21	4.48	8.55	9.93
$M_{i\infty}$ attenuated at gauge location	-	-	7.85	8.68
$M_{i\infty}$ maximum attenuation	8.48	3.17	7.12	8.27
M_{∞}	6.89	3.43	7.85	9.12

However, locally the Mach numbers could exceed this value due to the finite width gradient effect. In the nitrogen cases the measured Mach numbers* are quite close to M_{∞} while in the helium cases (where larger effects are consistently apparent) the Mach numbers are higher. The difference between the two gases is primarily due to the nature of the reflections on the contact surface. These reflections give rise to relatively strong compression waves when helium is used for both driver and test gases whereas when nitrogen is the test gas the reflected waves are weak (had the initial Mach number been smaller even the first reflected wave would have been a rarefaction fan). Hence in the nitrogen cases multiple reflected waves on the contact surface have little additional strengthening effect on the transmitted shock.

---

* After the gradient (Table II).

5.3 Summary

Figures 21a to d summarize the experimental data and the results of calculations of the different phenomena involved. Since in the experiments all characteristic lengths are comparable (Table III) the results are presented in terms of a nondimensional length $\bar{x}_L = (x/L - 1)$. However, each data point corresponds to a different relative influence of the respective wave systems. Table VI presents a similar summary.

TABLE VI

M_{mea} / ρ'_1/ρ_1	2.36/68.6	2.36/3.88	5.13/3.88	5.74/3.88
M_T (Paterson)*	3.92	2.94	7.05	7.94
M_{max} (numerical computation)	5.50	3.1	7.24	8.12
M_{cw}	5.9	3.1	7.3	8.3
M_F *	5.56	3.36	7.78	9.02
M_∞	6.89	3.43	7.85	9.12
M'_{mea} (at end of gradient)	7.94	3.63	7.43	8.53
M'_{mea} (maximum)**	9.03	4.07	7.82	9.11
$M_{i\infty}$	11.21	4.48	8.44	9.93

*See Table V
**Measured Mach number furthest downstream of "gradient end."

As expected, figure 22a shows that the measured Mach numbers at $\bar{x}_L \sim 0$ are approximately $M_{max} + (M_F - M_T)$.

Due to the effect of subsequent multiple reflected waves on the contact surface, the Mach number then increases. Within the measurement range the expected eventual decrease towards M_∞ is not observed.

Similar comments apply to figure 21b. Here, however, the first interaction (D on figures 20 and 21b) occurs for $\bar{x}_L > 1$. This distance is considerably reduced by viscosity since (Table III) $\ell_m \lesssim \ell_a/2$ and the Mach number increase due to "contact surface effects" indeed occurs near $\bar{x}_L \sim 0$.

Figures 21c and d are essentially similar. In these cases ℓ_m and ℓ_a are of the same order. Hence the predicted location of the first interaction is approximately correct. The measured data first display mainly the direct effect of the gradient ($M'_{mea} \sim M_{max}$), with only a slight contribution from the compression wave reflected on the contact surface. A larger effect is noticed at the location of the first (idealized) interaction where the measured value approximately equals $M_{max} + (M_F - M_T)$. Since $M_F \sim M_\infty$ for these cases further interactions are of little consequence. In figure 21d the relative magnitude of ℓ_a and ℓ_m (Table III) again shifts the data pattern towards $\bar{x}_L = 0$, as occurred for the helium-LN_2 case.

In all cases, and in spite of the approximations of a discontinuous density for the contact surface effects computations, the concepts of equivalent pressure ratios and scaling by the maximum test length for the viscous effects, and the importance of the waves reflected from the contact surface in predicting the strengthening of a shock propagating through a density gradient are confirmed by the data. Primarily as a consequence of the contact surface effects, the capability of obtaining very strong shocks in a cryogenic shock tube such as was used in these experiments has been thoroughly demonstrated.

VI CONCLUSION

The strengthening of shock waves by passage through a positive density gradient has been studied in a specially designed cryogenic shock tube. The capability of obtaining strong shocks with comparatively large test times in such an experimental configuration has been demonstrated. In the particular experiments performed, using a moderate diaphragm pressure ratio (1.2×10^3) and a normal driver temperature, shock Mach numbers larger than 9 with test times of the order of 80 μs have been measured in helium; this represents more than a factor of 3 increase from the case when the density is constant in the test section. This method of obtaining strong shock compares favorably with the explosive driver technique since here no part of the apparatus is damaged during tests.

Measurements after the gradient showed that the shock Mach number approached the limiting value corresponding to coincident pressure and temperature discontinuities (the value predicted to occur, in the absence of viscosity, infinitely far from both the diaphragm and the density gradient). The mechanism by which such strong Mach numbers can be obtained for relatively wide gradients and short shock tubes has been explained. The propagation of a shock in a shock tube through a positive density gradient combines the effects of the primary shock-gradient interaction with the equally large (for suitable initial conditions) effects due to waves reflected on the contact surface. In addition viscous effects become important in the presence of solid boundaries. The reduction in shock strength by viscous attenuation can be approximated by using an "equivalent pressure ratio" corresponding to the strength of the shock as it enters the gradient. (This can be either measured or approximated from Mirel's shock attenuation computation, Ref. 22). The latter two effects were not accounted for in previous theoretical treatments of the problem; however, their spatial scale may be such that they cannot be neglected. For the experimental conditions considered the contact surface effects dominated the shock-gradient interaction by the end of the nonuniform region. Moreover due to the influence of viscosity the maximum shock strength occurs within a few gradient widths beyond the gradient end.

An example of a case where similar effects can be expected is that of a body moving at supersonic speed through an increasingly dense medium. Larger increases in shock strength may occur than predicted by considering the shock-gradient interaction independent of the body; the resulting effect on the body may be critical.

It would be interesting to expand the available numerical solutions of the shock-gradient interaction to account for other flow nonuniformities behind the incident shock. Local shock strengths for specific initial conditions (in particular the maximum shock Mach number) could then be determined more accurately, allowing a more efficient use of the cryogenic shock tube.

However, in its present form this system can be used for further experimentation. Potential applications include the effect of heat pulses on superconducting materials and phenomena related to "second sound" in liquid helium. With higher initial pressure ratios and heated drivers, stronger shocks can easily be obtained without undue restrictions on the test time. Since Mach number amplification is enhanced by the use of a light gas, this method may also be useful in studying phenomena related to supersonic entry into light gas atmospheres.

APPENDIX A

Ideal Gas Shock Relations

A. 1 Shock Jump Equations

The equations relating the thermodynamic and flow variables on either side of a shock wave can be found in numerous references (e.g. 18). They are summarized below for ideal gases. Conditions upstream of the shock are denoted by the subscript 1, downstream by the subscript 2. M is the shock Mach number, and the variables are defined in terms of a lab-fixed frame of reference.

$$\frac{\rho_2}{\rho_1} = \frac{(\gamma+1)\,M^2}{(\gamma-1)M^2+2} \qquad \text{density}$$

$$\frac{p_2}{p_1} = \frac{2\gamma\, M^2-(\gamma-1)}{\gamma+1} \qquad \text{pressure}$$

$$\frac{T_2}{T_1} = \left(\frac{a_2}{a_1}\right)^2 = 1 + \frac{2(\gamma-1)}{(\gamma+1)^2}\,\frac{(M^2-1)(1+\gamma M^2)}{M^2} \qquad \text{temperature (speed of sound)}$$

$$\frac{u_2-u_1}{a_1} = \frac{2}{\gamma+1}\,\frac{M^2-1}{M} \qquad \text{velocity}$$

where by convention the velocity of the shock ($U = Ma_1$) with respect to the fluid into which it propagates is positive.

For strong shocks these equations reduce to:

$$\frac{\rho_2}{\rho_1} = \frac{\gamma+1}{\gamma-1}$$

$$\frac{p_2}{p_1} = \frac{2\gamma}{\gamma+1}\,M^2$$

$$\frac{T_2}{T_1} = \left(\frac{a_2}{a_1}\right)^2 = 2\gamma \frac{\gamma-1}{(\gamma+1)^2} M^2$$

$$\frac{u_2-u_1}{U} = \frac{2}{\gamma+1}$$

A. 2 The Shock Tube Equation

The shock Mach number produced by a given pressure ratio p_4/p_1 across the diaphragm of a shock tube, with a driver gas at conditions 4 and a test gas at conditions 1, is given by

$$\frac{p_4}{p_1} = \frac{1 + \frac{2\gamma_1}{\gamma_1+1}(M^2-1)}{\left[1 - \frac{\gamma_4-1}{\gamma_1+1} \frac{a_1}{a_4} \frac{M^2-1}{M}\right]^{\frac{2\gamma_4}{\gamma_4-1}}}$$

APPENDIX B

Computation Procedure for the Shock-Gradient Interaction

The computations of the shock-gradient interaction are made with the assumptions outlined in Part II. An initial shock wave propagates through a uniform density region in a one-dimensional shock tube. At $x = 0$ it encounters a density gradient* extending to $x = L$. The uniform flow behind the initial shock is assumed to extend upstream to infinity.

The flow behind the shock is described by equations (3-5) in section 2.1.2. Across the shock the relationships from Appendix A must hold, and along the shock $\frac{dx}{dt} = U = Ma_1$. The equations of motion are numerically integrated in the physical plane following the method used by Keller et al. (Ref. 34).

The variables are normalized using the initial pressure (p_1), temperature (T_1), and gradient length L in the following way:

$$\bar{x} = \frac{x}{L}$$

$$\bar{t} = \frac{t\sqrt{\gamma R_g T_1}}{L}$$

$$\bar{\rho} = \frac{R_g T_1}{p_1} \rho$$

$$\bar{p} = \frac{p}{\gamma p_1}$$

---

*The pressure is constant (hydrostatic pressure variations due to gravity in the experiments were on the order of $10^{-5}\ p_1$)

$$\overline{T} = \frac{T}{T_1}$$

$$\overline{u} = \frac{u}{\sqrt{\gamma R_g T_1}} \qquad \overline{U} = \frac{U}{\sqrt{\gamma R_g T_1}} \qquad M = \frac{\overline{U}}{\overline{T}'^{\frac{1}{2}}_1}$$

where R_g is the test gas constant.

Combining and normalizing the equations, the set of equations to be numerically integrated becomes:

$$\left.\begin{aligned}
&(1)\quad \frac{\partial\overline{\rho}}{\partial\overline{t}} + \frac{\partial\overline{\rho}\,\overline{u}}{\partial\overline{x}} = 0 \\
&(2)\quad \frac{\partial\overline{u}}{\partial\overline{t}} + \frac{1}{2}\frac{\partial\overline{u}^2}{\partial\overline{x}} = -\frac{1}{\overline{\rho}}\frac{\partial\overline{p}}{\partial\overline{x}} \\
&(3)\quad \frac{\partial\overline{p}}{\partial\overline{t}} + \frac{\partial\overline{p}\,\overline{u}}{\partial\overline{x}} + (\gamma-1)\, p\, \frac{\partial\overline{u}}{\partial\overline{x}} = 0
\end{aligned}\right\}\ \text{behind the shock}$$

$$\left.\begin{aligned}
&(4)\quad \overline{\rho} = \frac{1}{\overline{T}'_1}\,\frac{(\gamma+1)M^2}{(\gamma-1)M^2+2} \\
&(5)\quad \overline{u} = \overline{T}'^{\frac{1}{2}}_1\,\frac{2}{\gamma+1}\,\frac{M^2-1}{M} \\
&(6)\quad \overline{p} = \frac{2\gamma M^2-(\gamma-1)}{\gamma(\gamma+1)}
\end{aligned}\right\}\ \text{across the shock}$$

$$(7)\quad \frac{d\overline{U}}{dt} = \frac{\overline{U}^2}{2\overline{T}'_1}\,\frac{d\overline{T}'_1}{d\overline{x}} + \frac{\gamma+1}{4}\,\frac{\overline{T}'_1}{\overline{U}}\left\{(\overline{U}-\overline{u})\frac{\partial\overline{p}}{\partial\overline{x}} - \gamma\overline{p}\,\frac{\partial\overline{u}}{\partial\overline{x}}\right\} \quad \text{along the shock}$$

with the boundary conditions

$\overline{p}_1 = 1/\gamma$ for all $\overline{x}$

$M = M_I \qquad \overline{x} < 0$

$\overline{T}'_1 = 1 \qquad \overline{x} < 0;$ given function of $\overline{x}$ for $\overline{x} > 0$

Equations (1), (2), (3) are solved using forward $\bar{t}$ differences and centered $\bar{x}$ differences on an $(\bar{x}, \bar{t})$ net.

Typically, equation (2) is solved as follows:

$$U(I,J) = \frac{1}{2}\left[U(I+1,J-1) + U(I-1,J-1)\right] -$$

$$\left[U^2(I+1,J-1) - U^2(I-1,J-1)\right] \frac{\Delta T}{2\Delta X}$$

$$- \frac{1}{R(I,J-1)} \left[P(I+1,J-1) - P(I-1,J-1)\right] \frac{\Delta T}{2\Delta X}$$

Backward $\bar{t}$ differences are used when the shock is encountered, and the equations solved by iteration simultaneously with equations (4-7). The iteration is stopped when the percentage change in $\bar{U}$ is less than a fixed value.

The net was chosen so that $\Delta\bar{t} = \Delta\bar{x}/2M_I$. Computations were quite sensitive to the choice of $\Delta\bar{x}$. A value of 5×10^{-3} was used for all the computations such as those presented on figures 5 and 19, since less than a 1% change in the maximum Mach number resulted from halving this value. Figure 22a shows the net used, and figure 22b summarizes the main program steps (figure 22b is not the actual flow diagram of the program).

APPENDIX C

Detailed Description of the Experimental Apparatus

C.1 Shock Tube Description

The basic shock tube configuration is shown in figure 7 and discussed in section 2.1.

The 1.5 in. i.d. stainless steel part of the test section extended 40.25 in. below the support plate. It was smoothly inserted into a 1.5 in. i.d. x 2.25 in. o.d. Shelby steel tube by increasing the inside diameter of a 1.5 in. section of the thicker tube. The thicker tubing was used to provide support for the side wall gauges. Since the coefficient of thermal conductivity for Shelby steel is .65w/cm°K compared to .115w/cm°K for stainless steel, this tubing helped to maintain the upper test section at room temperature.

A 1.5 in. ball valve was mounted at 11.5 in. above the support plate (just above the Shelby tubing). In addition to preventing condensation during diaphragm change, it was used to evacuate the lower test section before re-immersion in the coolant if the bottom gauges required replacement. An additional 30 in. brass section separated the side wall gauges from the diaphragm. This length was sufficient to remove any perturbations of the flow due to the diaphragm rupture. With a large thermal conductivity coefficient of .855 w/cm°K. it helped maintain the upper test section at a uniform (room) temperature. Finally, another short section of thick Shelby tubing was machined to hold the knife edges used to cut the diaphragm (Ref. 23). This piece also contained the main pumping port for the test section.

Except for the bottom flange seal, all vacuum seals used commercial O-rings. The bottom seal was made with .03 in. indium solder laid in a circular groove; the joining ends were cut at an angle to provide a seal without overlap. The groove was machined in a 1/4 in. thick stainless steel end wall. Eight bolts joining the test section end flange and this end wall were torqued to a level sufficient for the indium to cold flow.

The portions of the test section above and below the ball valve were independently valved to a manifold connected to pressure gauges. A 21.5 liters/sec Kinney pump was used to evacuate both portions. In addition an MCF60 diffusion pump was connected to the upper test section and was used to clean the shock tube between runs.

The driver was made of 1.5 in. i.d. brass tubing. Its 10 in. length was sufficient to prevent the reflected expansion wave from overtaking the contact surface within the shock tube length. The driver was connected to its pressure gauge and a common vacuum/gas inlet line with flexible tubing to allow its removal when changing the diaphragm.

Mylar was initially used as a diaphragm material, providing driver pressures of 50 to 60 in. Hg. However, the burst pressure was not sufficiently repeatable. Soft aluminum .003 in. thick was found to be better suited for this experiment. The knife blade position was adjusted to obtain both a repeatable burst pressure (95 psia) and clean diaphragm ruptures.

C. 2 Shock Velocity Gauges

C. 2. 1 Thin Film Side Wall Gauges (Incident Shock Velocity)

Thin film side wall gauges were used to determine the shock speed upstream of the gradient. These gauges consisted of thin platinum strips (resistance ~ 120 ohms) baked on 1/4 in. glass rods. Voltage dividers were built into cases surrounding the glass supports (fig. 7) and were powered by a common 24v supply. The gauge signals were amplified by high-gain linear or differentiating amplifiers and fed to a Hewlett Packard megacycle counter (Model 5233L). Gauge signals on the order of a millivolt were obtained using helium as the test gas, whereas stronger signals were obtained when nitrogen was used.

C. 2. 2 Filament and Slide Gauges (Final Shock Velocity)

The shock speed beyond the density gradient was measured by timing the shock passage at two precisely known locations.

Filament Gauge

The original gauge used (fig. 8, left) was similar to the gauges used in Ref. 25. Two 2mm diameter, 4 in. long glass needles were epoxied 3/4 in. apart in the test section end wall. Glass rather than metal needles were used to minimize thermal contraction and to insulate the gauge elements from the supports. Thin (0. 005 to 0. 010 in.) pyrex filaments coated with a platinum film were epoxied across the needle. Because the filaments often broke due to the impact of shreds of the diaphragm material, two pairs of filaments were installed to allow for redundancy (although only one pair was normally used). The breakage problem was alleviated by stringing a thin copper wire across the needles, to act as a shield.

Electrical continuity from the filaments to copper wires running along the needles was provided by silver print. The copper wires were in turn soldered to a Latronics multiheader terminal (type 97. 3508) inserted in the end wall.

Although the filament gauge proved sensitive and yielded excellent results, the need to frequently replace it led to the development of an alternate method of measuring shock velocity.

Thin Film Slide Gauge

The basic gauge arrangement is similar to the preceding case but here thin films replace the filaments. Two platinum films were baked on a glass slide (fig. 8, right) having a sharp leading edge. Electrical continuity with the platinum films was achieved by silver print between the films and indium soldered to the glass. The indium in turn was soldered to the copper lead out wires. The indium was used to minimize the differential thermal contraction between the copper wires and the glass, which resulted in flaking of the silver print. The ratio of the slide cross sectional area to that of the shock tube was 2.3%. The one-dimensional theory on shock strengthening due to area contraction (Ref. 3) predicts an effect on the order of $\Delta M/M \sim .4\%$ in N_2 and .5% in He (negligible compared to the strengthening due to the temperature gradient).

Measurement Technique

Power for either type of gauge was provided by a pulse generator through voltage dividers. The pulse was triggered by the passage of the shock across the lower side wall gauge element, and resulted in a 2.5v pulse through the gauges. The duration of the pulse was set externally between 800 to 1000 μs. Thus the Joule heating in the gauges was kept at a minimum.

The output of the gauges was fed to a Tektronix 555 Oscilloscope with a type A17A differential amplifier plug-in unit. The resulting oscilloscope traces were recorded on film.

C. 3 Cryogenic System

To insure proper cooling of the LHe dewar, a 10 in. collar of styrofoam molded between concentric stainless steel walls was added to the LN_2 dewar (increasing the LN_2 dewar inside length to 38.5 in.). Liquid nitrogen could then be maintained 1 in. above the double walled section of the LHe dewar, reducing the LHe boil-off rate to a maximum of 2 in./hr. Figure 23 shows the boil-off rate in both the LN_2 and LHe dewar during gradient measurement tests.

Section 3.3 contains the principal characteristics of the dewars. The double-walled vacuum jacket of the LHe dewar was entirely silvered and could be evacuated through a stem and valve assembly extending 3.25 in. along the single-wall section (fig. 7). A collar, clamped around the solid-walled neck, was tightened to a master support plate* (figure 7a) holding the dewar in position. A gasket was placed in a groove molded on top of the neck to provide a vacuum seal. A pumping port in the neck was connected to the Kinney pump through a 2 in. gate valve. This connection was used to evacuate the dewar during the filling procedure. The pressure was monitored with a 0-200 psia manifold pressure gauge.

The liquid level was measured with a "dipstick" (Ref. 27) made from a 1/16 x 1/16 x 44 in. strip of balsa wood mounted on

---

*Both the LHe dewar collar and the shock tube support plate were attached to a master support plate.

a 1 in. thick styrofoam floater (partially visible in fig. 7c). The dipstick extended out of the dewar through the shock tube support plate into a lucite tube (fig. 7b). This tube was sealed at the support plate and at the upper end during LHe runs.

The shock tube support plate contained an LHe fill hole which was used as a vent during operations at liquid helium temperatures (and which could be sealed when necessary). It also included a 21 pin connector (Bendix) through which electrical continuity was maintained between gauges situated in the dewar and external measuring circuits.

C. 4 Gradient Measurements

A survey of low temperature thermometry showed that 1/8 watt Allen Bradley resistors had been calibrated over the required temperature range of 4.2°K to 300°K (Refs. 26 and 27).

Resistors in the nominal range of 300 to 500 ohms were obtained and calibrated at ambient, liquid nitrogen and liquid helium temperatures to determine the necessary constants (section 3.4). A check on the calibration accuracy was made at liquid argon temperature. A typical calibration is plotted in figure 24, and shows that the resistors are very sensitive thermometers below 100°K but less sensitive for higher temperatures. The calibrations on a set of resistors were checked after a gradient measurement test.* Changes in the calibration constants resulted in less than a 2% change in the temperature data.

The resistors were mounted at fixed locations on a balsa wood frame which centered them in the shock tube test section during the gradient measurements. Electrical continuity was provided by varnish-insulated #32 wires with a common ground. A feed-through section was designed with two hermetically-sealed connectors to interface with the upper shock tube. This section was used in lieu of the driver for the gradient measurements. A Hewlett Packard digital multimeter was used to measure

---

*Although the absolute resistance of a carbon resistor changes after thermal cycling, the ratio of resistances for any two given temperatures is relatively constant (Refs. 26 and 27). The change in resistance ratios as a consequence of thermal cycling corresponds to absolute temperature errors of 0.11°K (at 4.2°K) to 0.5°K (at 77.4°K).

resistances. No more than 5×10^{-6} joules per measurement were dissipated in the resistors at liquid helium temperature. This heating was allowed to increase to 5×10^{-3} joules for resistors at or above liquid nitrogen temperature. The external circuit resistance was measured so as to obtain accurate values for individual resistors.

The presence of the frame and copper wires slightly perturbed the initial temperature distribution. Because the thermal conductivity of balsa wood is quite low (its ambient thermal conductivity is less than that of glass), the primary source of additional heat flow due to the "resistor ladder" was the electrical leads. These leads were soldered to a connector maintained at room temperature, and heat conduction along these leads would tend to increase the temperature at any position within the shock tube. However, the ratio of heat conduction along a wire (connected to a resistor in the 4.2°K region of the test section) to the heat conduction along the test section walls was calculated to be less than 1%. Temperature data taken with the resistors at different locations (resulting in different heat flow patterns due to the copper wires) showed no significant differences.

REFERENCES

1. Chester, W., Phil. Mag. (7) 45, 1293 (1954).
2. Chisnell, R.F., J. Fluid Mech. 2, 286 (1957).
3. Whitham, G.B., J. Fluid Mech. 4, 337 (1958).
4. Guderley, G., Luftfahrtforschung 19, 302 (1942).
5. Butler, D.S., Armament Research Establishment Report 54/54 (1954).
6. Russell, D.A., J. Fluid Mech. 27, 305 (1967).
7. Setchell, R.E., Ph.D. Thesis, California Institute of Technology (1971).
8. Raizer, Y., Soviet Physics 8, 1056 (1963).
9. Hayes, W.D., J. Fluid Mech. 32, 305 (1968).
10. Sakurai, A., Comm. Pure Appl. Math. 13, 353 (1960).
11. Sedov, L.I., Similarity and Dimensional Methods in Mechanics (1954).
12. Ono, Y., Sakashita, S., and Yamazaki, H., Progr. Theor. Phys. 23, 294 (1960).
13. Nadezhin, D.K. and Frank-Kamenetski, D.A., Soviet Astronomy-AJ 9, 226, (1965).
14. Chisnell, R.F., Proc. Royal Soc., Series A 232, 350 (1955).
15. Bird, G.A., J. Fluid Mech. 11, 180 (1961).
16. Landau, L.D. and Lifshitz, E.M., "Fluid Mechanics" Pergamon Press (1959).
17. Paterson, S., Proc. Phys. Soc., 61, 119 (1948).
18. Glass, I.I. and Patterson, G.N., J. Aero. Sc., 22, 73 (1955).

REFERENCES (cont.)

19. Rudinger, G., "Wave Diagrams for Nonsteady Flow on Ducts." D. Van Nostrand (1955).

20. Von Neumann, J., OSRD Report #1140 (1943).

21. Roshko, A., Phys. Fluids 3, 835 (1960).

22. Mirels, H., Phys. Fluids 7, 1208 (1964).

23. Roshko, A., and Baganoff, D., Phys. Fluids 4, 1445 (1961).

24. Sturtevant, B., and Slachmuylders, E., Phys. Fluids 7, 1201 (1964).

25. Babiskin, J., Rev. Scient. Instrum. 21, 941 (1950).

26. Schulte, E. H., Cryogenics 6, 321 (1966).

27. Brocherds, P.H., Cryogenics 9, 128 (1969).

28. "Argon, Helium and the Rare Gases," G. A. Cook Ed., Interscience Publishers (1961).

29. Stewart, R. B., et al., NBS Ad272769, 111 (1961).

30. White, D. R., J. Fluid Mech. 4, 585 (1958).

31. Mirels, H., Phys. Fluids 6, 1201 (1963).

32. Mirels, H., AIAA J. 2, 84 (1964).

33. Roshko, A., and Smith, J. A., AIAA Journal 2, 186 (1964).

34. Keller, H. B., Levine, D. A., and Whitham, G. B., J. Fluid Mech. 7, 302 (1960).

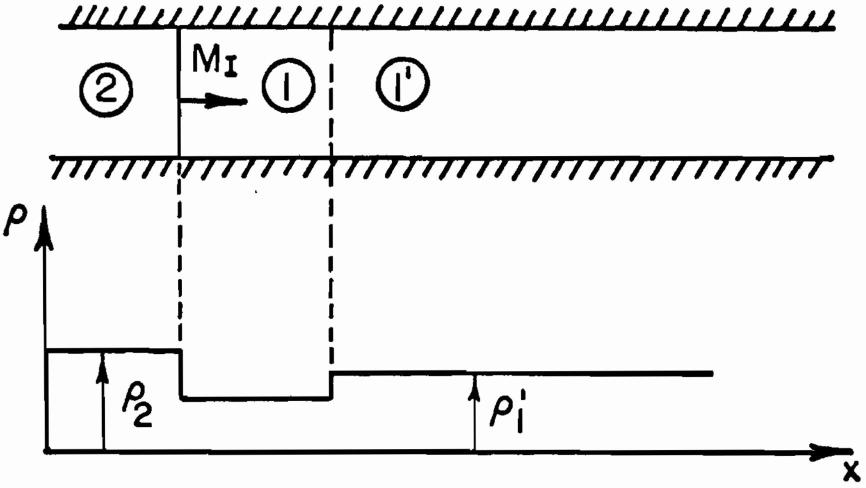

Ia BEFORE INTERACTION

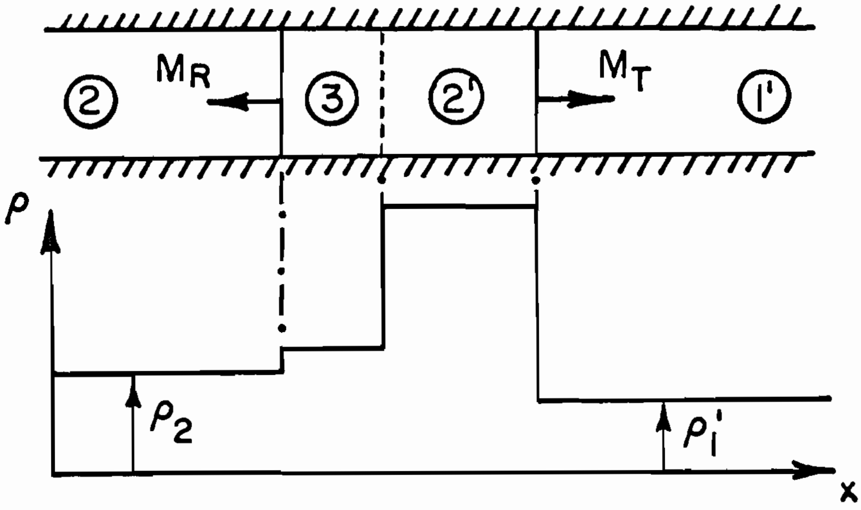

I b AFTER INTERACTION

Not to scale

FIG. I INTERACTION OF A SHOCK WITH A DENSITY DISCONTINUITY.
DENSITY DISTRIBUTION.

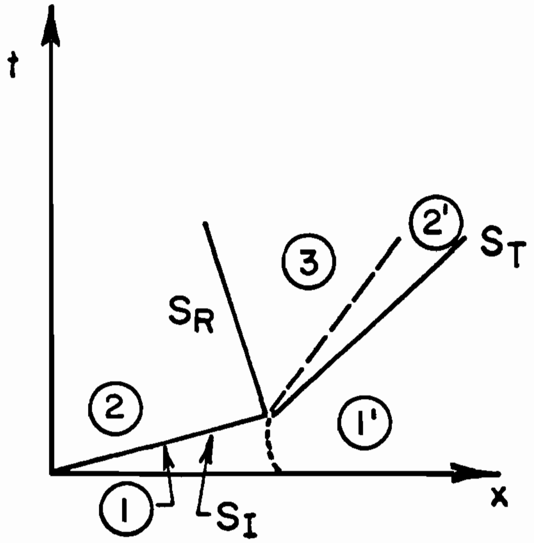

2a SHOCK PATH

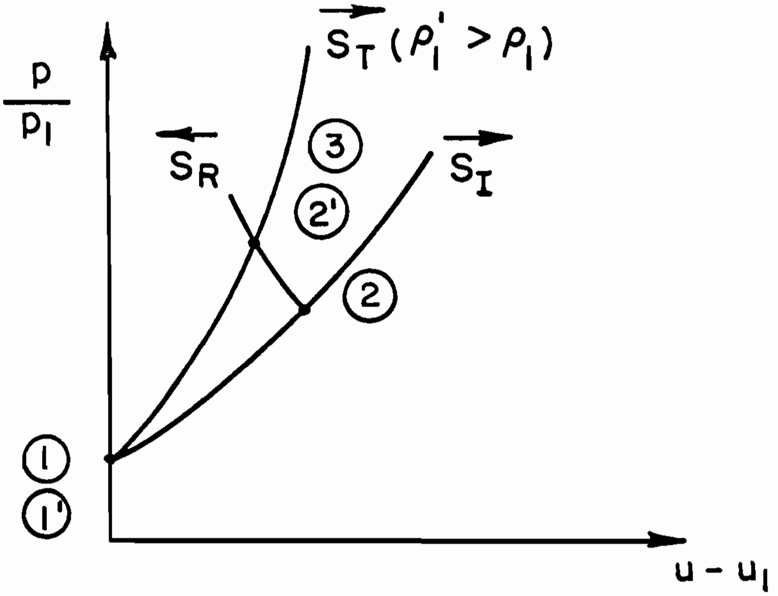

2b PRESSURE-VELOCITY DIAGRAM

FIG. 2 INTERACTION OF A SHOCK WITH A DENSITY DISCONTINUITY

Not To Scale

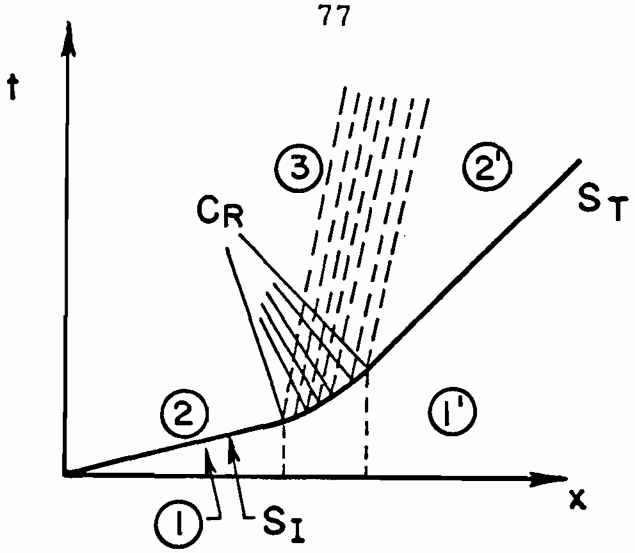

3a WAVE PATHS

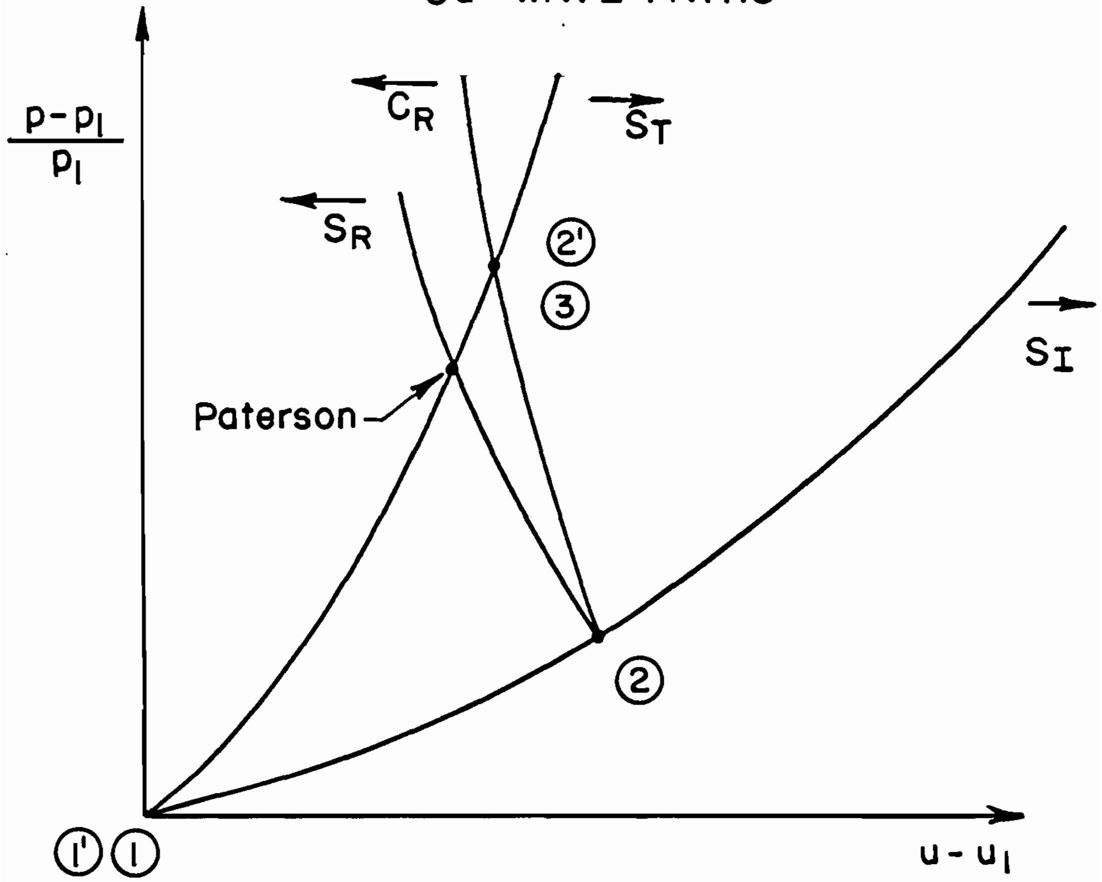

3b PRESSURE-VELOCITY DIAGRAM

FIG. 3 INTERACTION OF A SHOCK WITH A FINITE WIDTH DENSITY GRADIENT
(Re-reflected waves neglected)

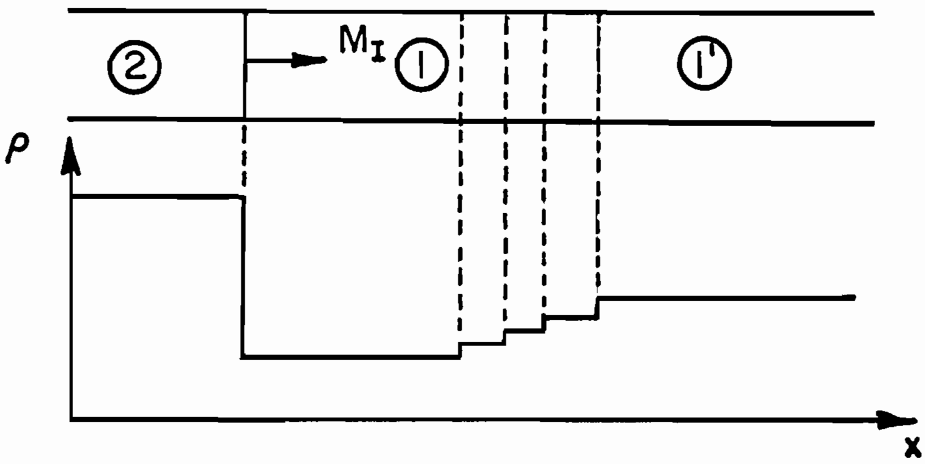

4a APPROXIMATE DENSITY DISTRIBUTION BEFORE INTERACTION

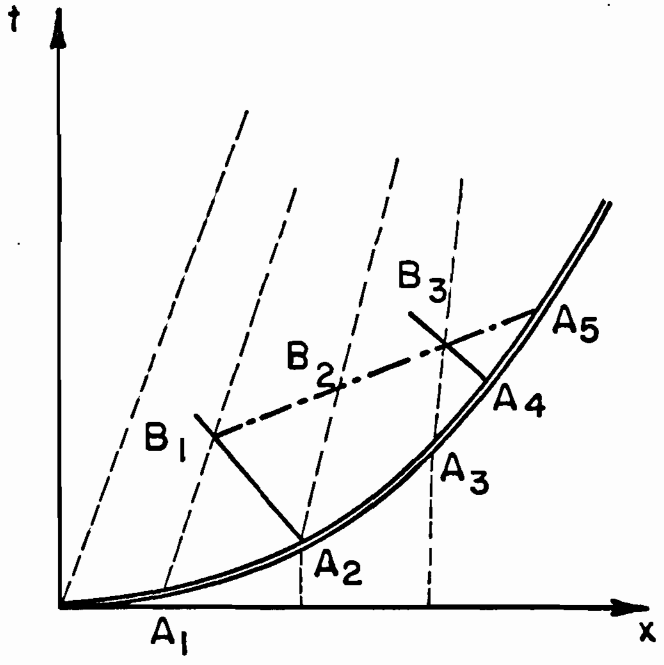

4b WAVES PATHS (TYPICAL)

═══ SHOCK

——— REFLECTED WAVE

------ PARTICLE PATH

—·—·— RE-REFLECTED WAVE

FIG. 4 INTERACTION OF A SHOCK WITH A SUCCESSION OF WEAK DISCONTINUITIES

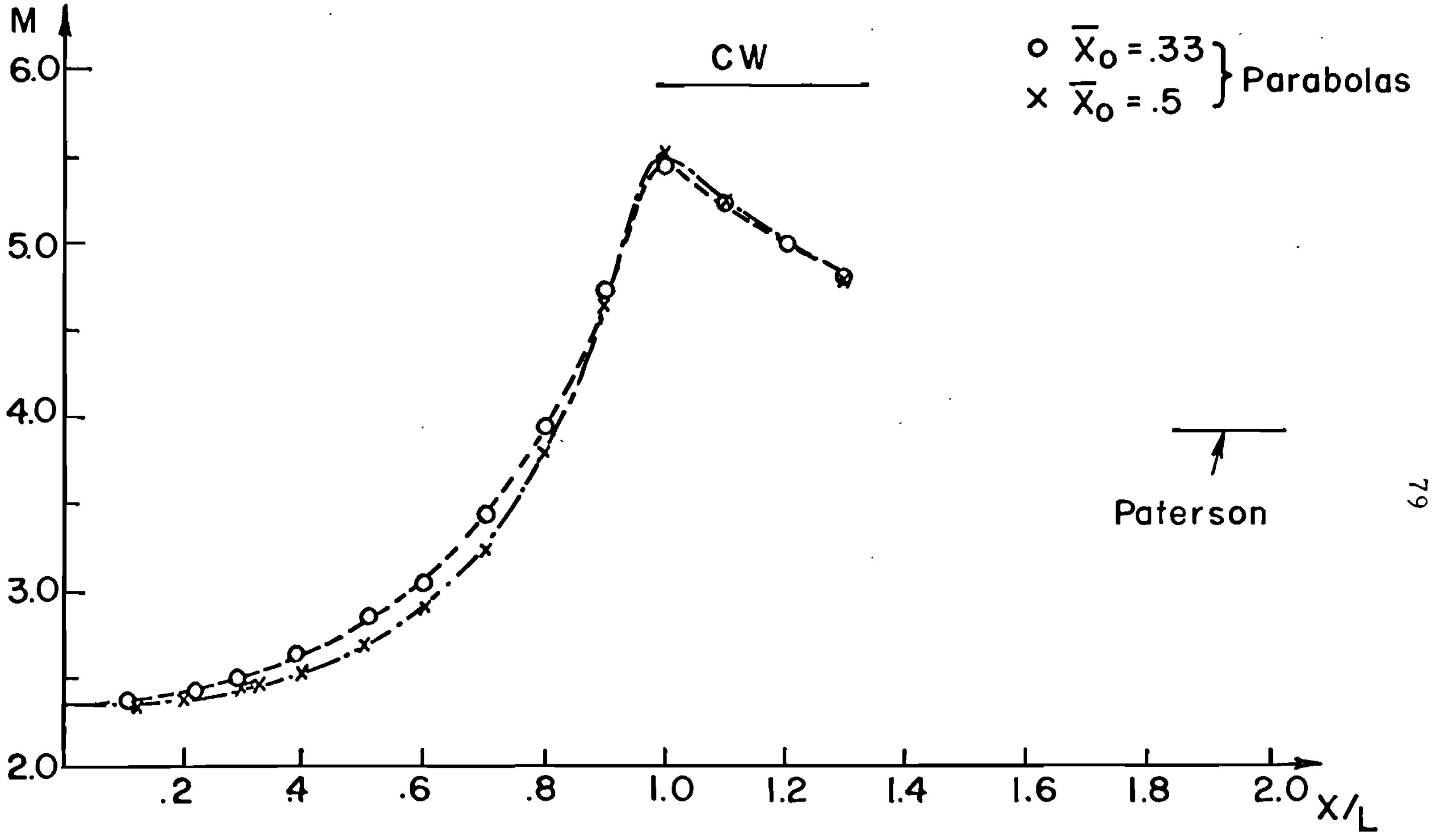

FIG. 5 PARABOLIC GRADIENT He SHOCK – $\rho_1'/\rho_1 = 68.6$

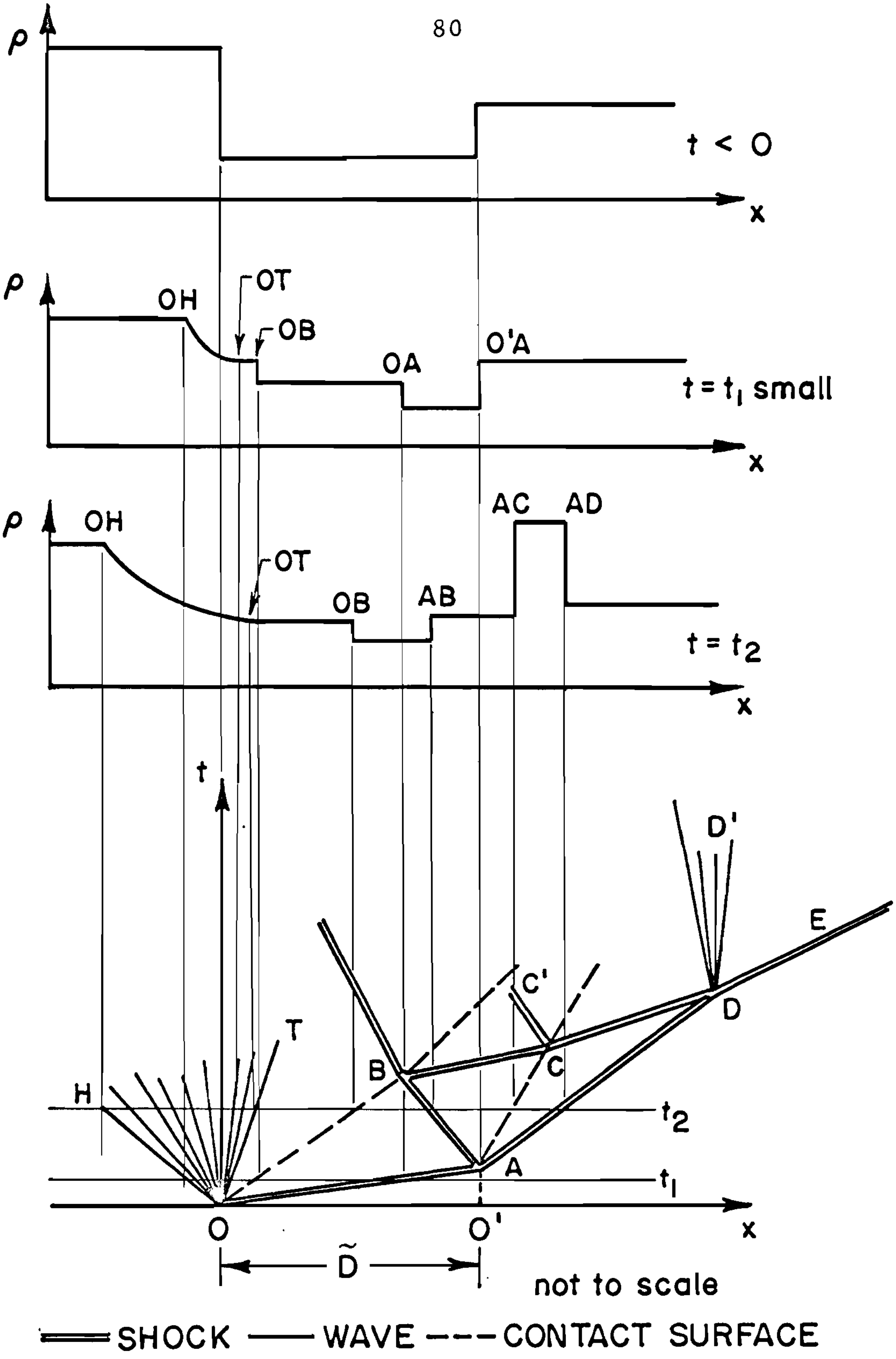

FIG. 6 SHOCK TUBE WITH A DENSITY DISCONTINUITY

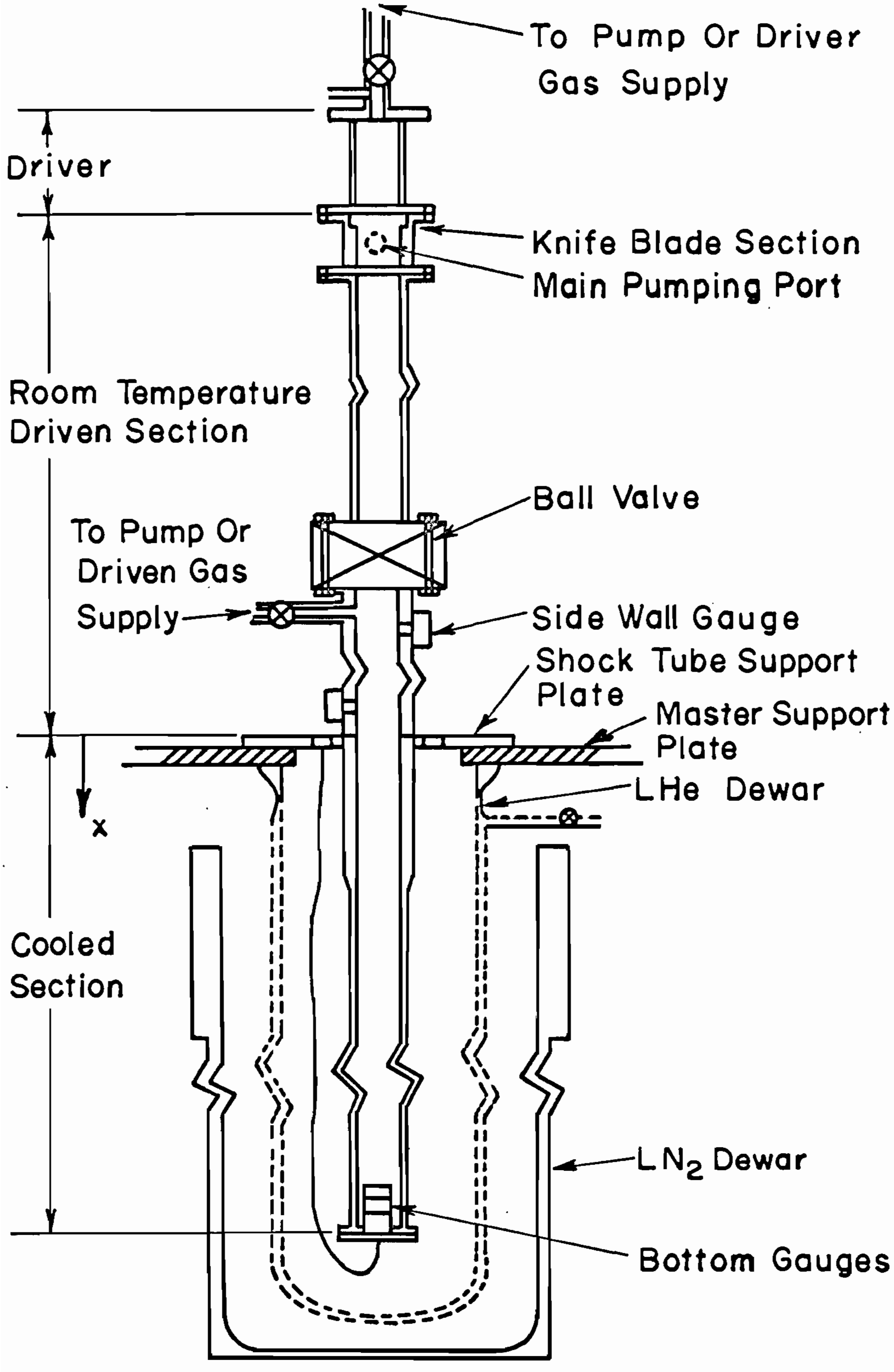

FIG.7a SCHEMATIC DIAGRAM CRYOGENIC SHOCK TUBE

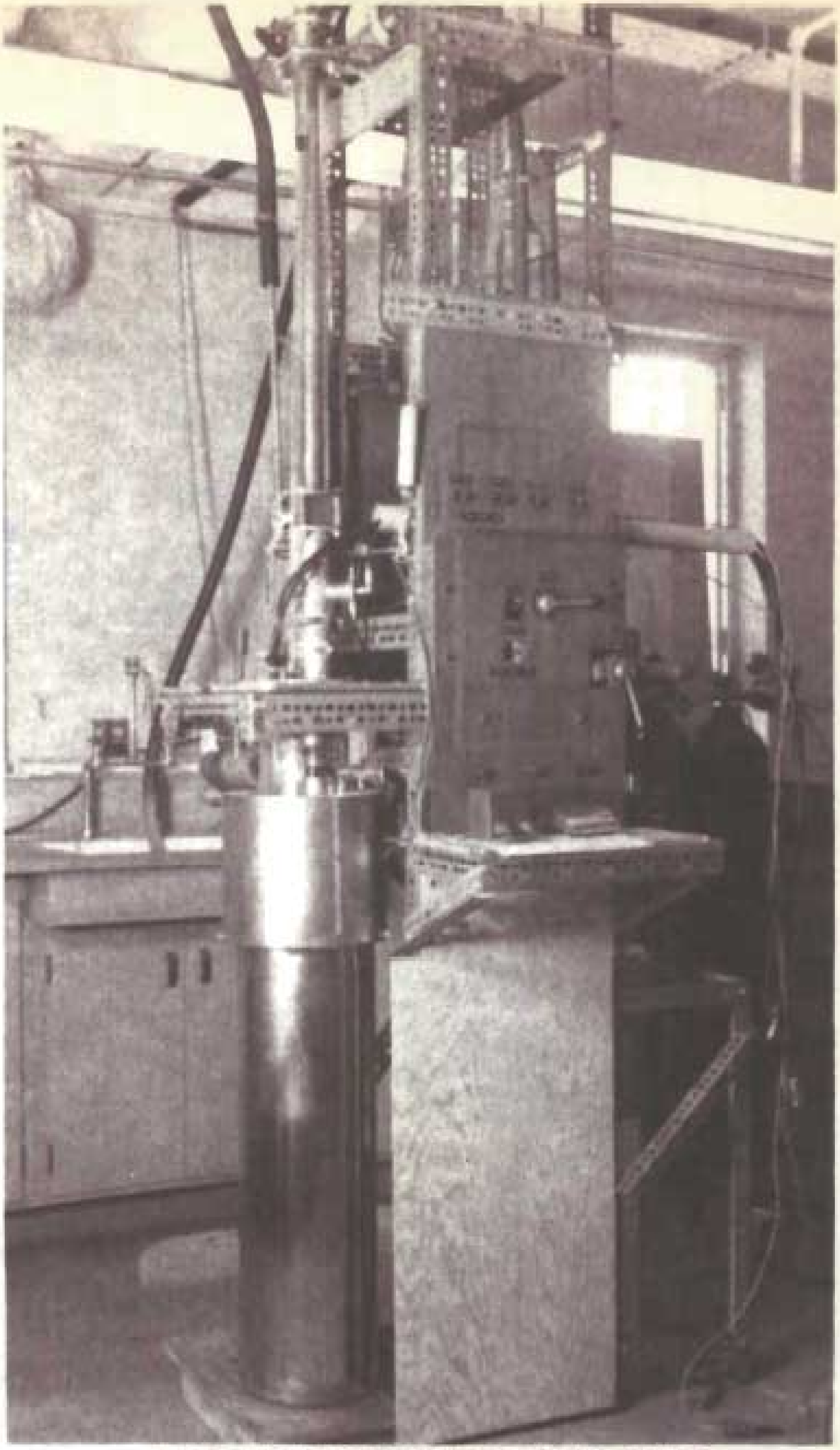

FIG. 7b CRYOGENIC SHOCK TUBE

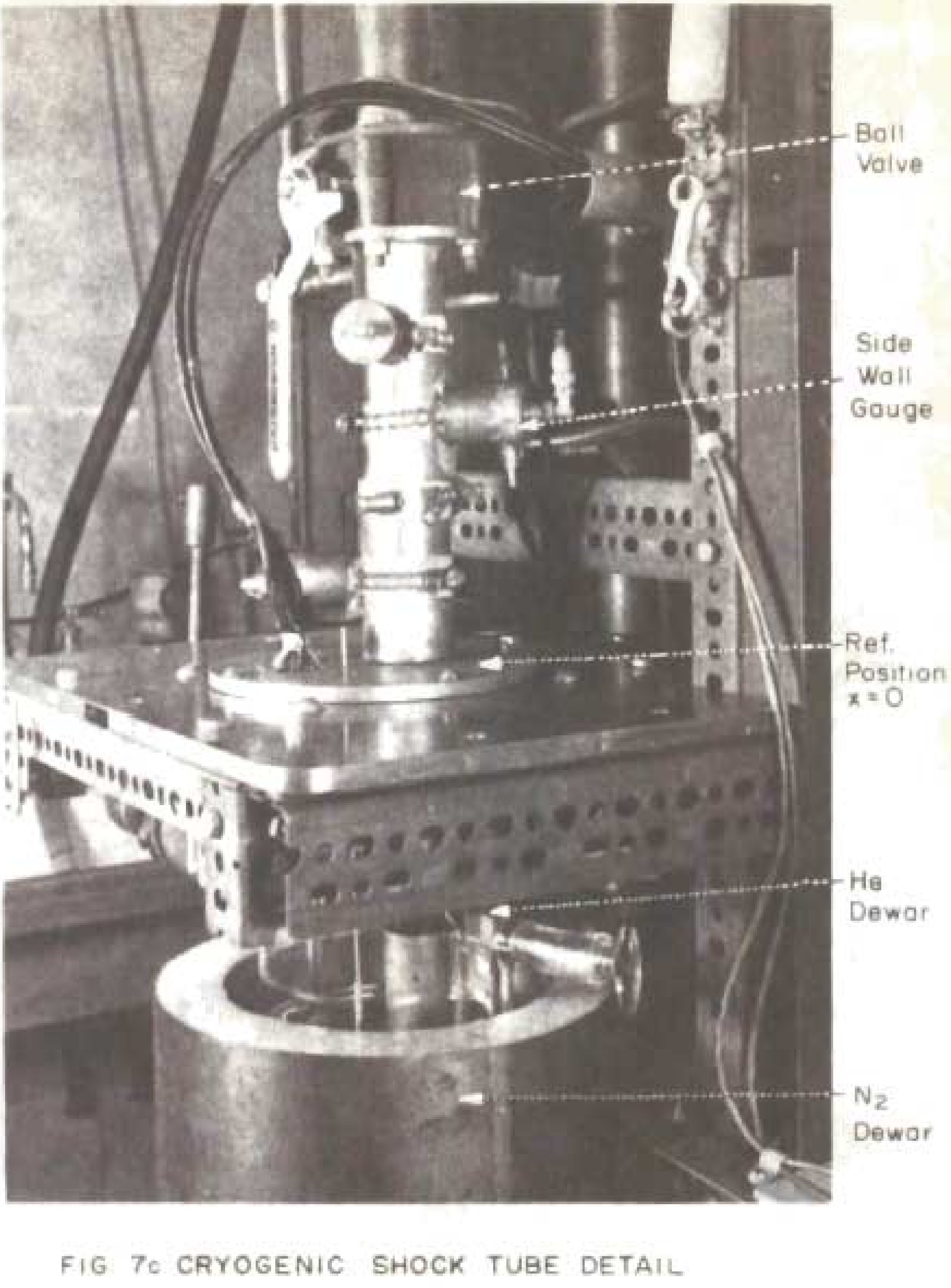

FIG 7c CRYOGENIC SHOCK TUBE DETAIL

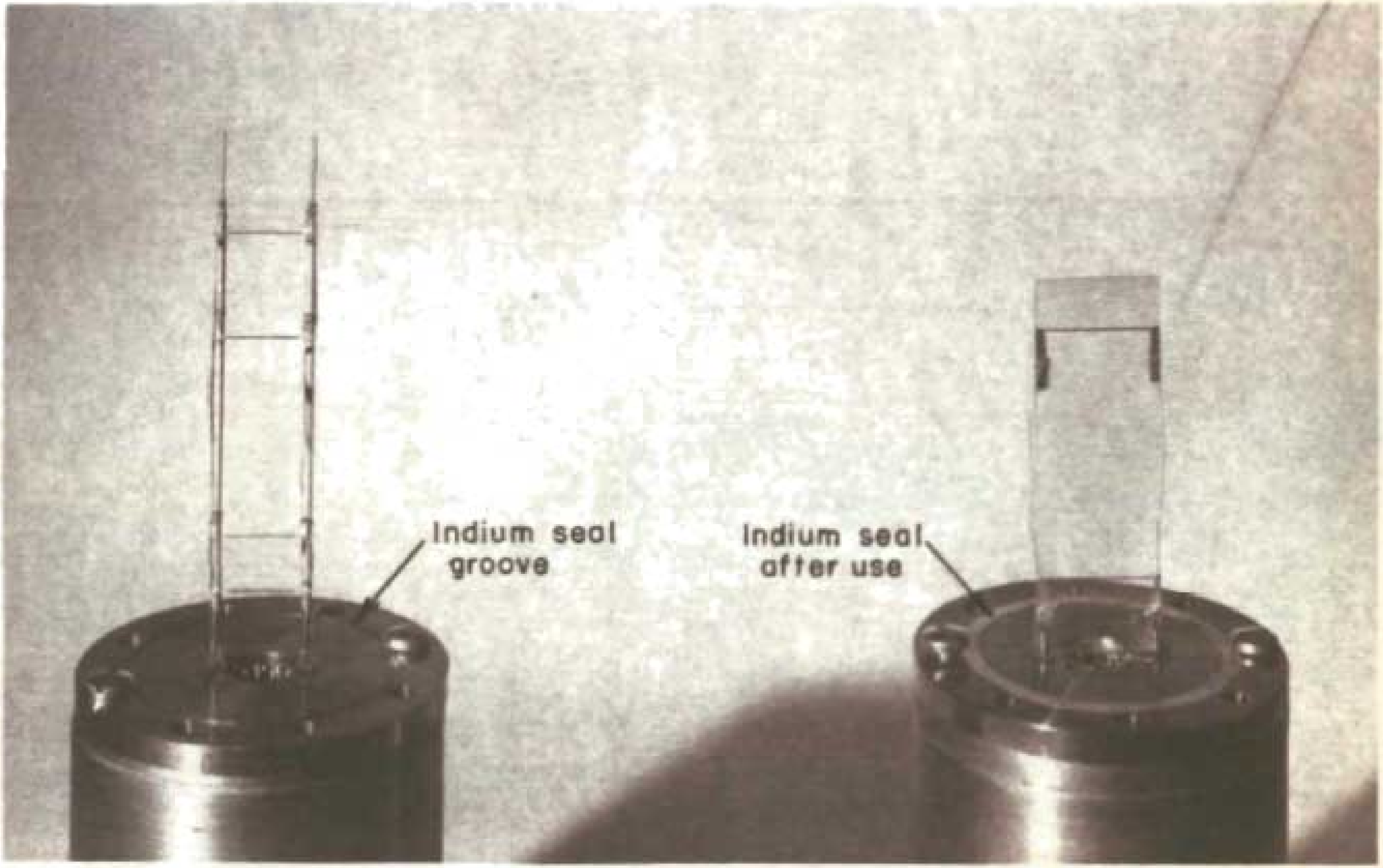

Filament Gauge "Slide" Gauge

FIG. 8 LOWER VELOCITY GAUGES

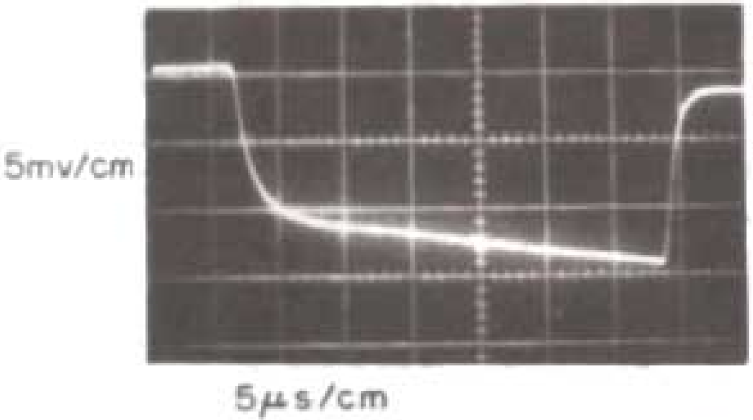

FIG. 9a M=5.74 (N_2), LN_2 COOLANT

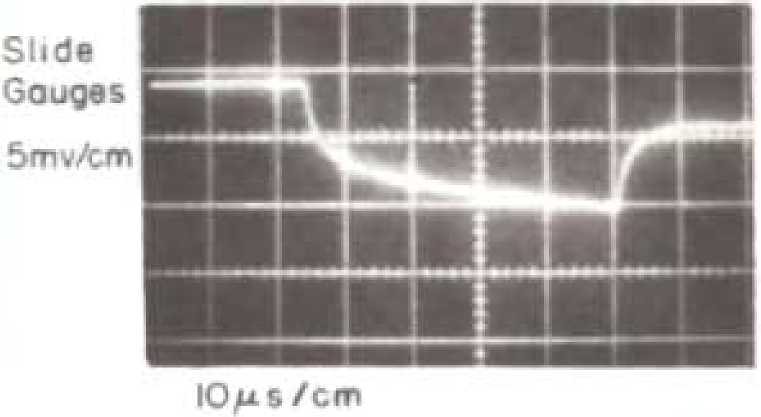

FIG. 9b M=2.36 (He), LHe COOLANT

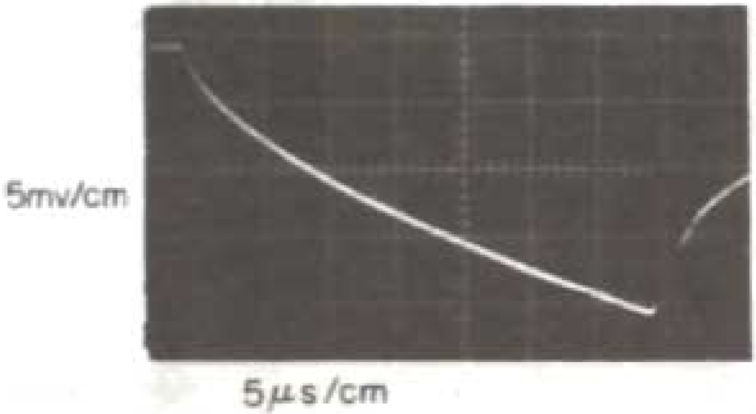

FIG. 9c M=2.36 (He), LN_2 COOLANT

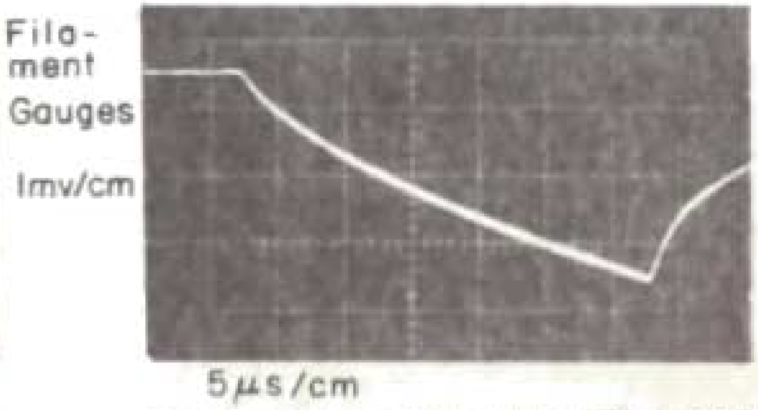

FIG. 9d M=2.36 (He), NO COOLANT

FIG. 9 GAUGE RESPONSES (DIFFERENTIAL AMPLIFICATION)

M Is The Mach Number Before The Gradient

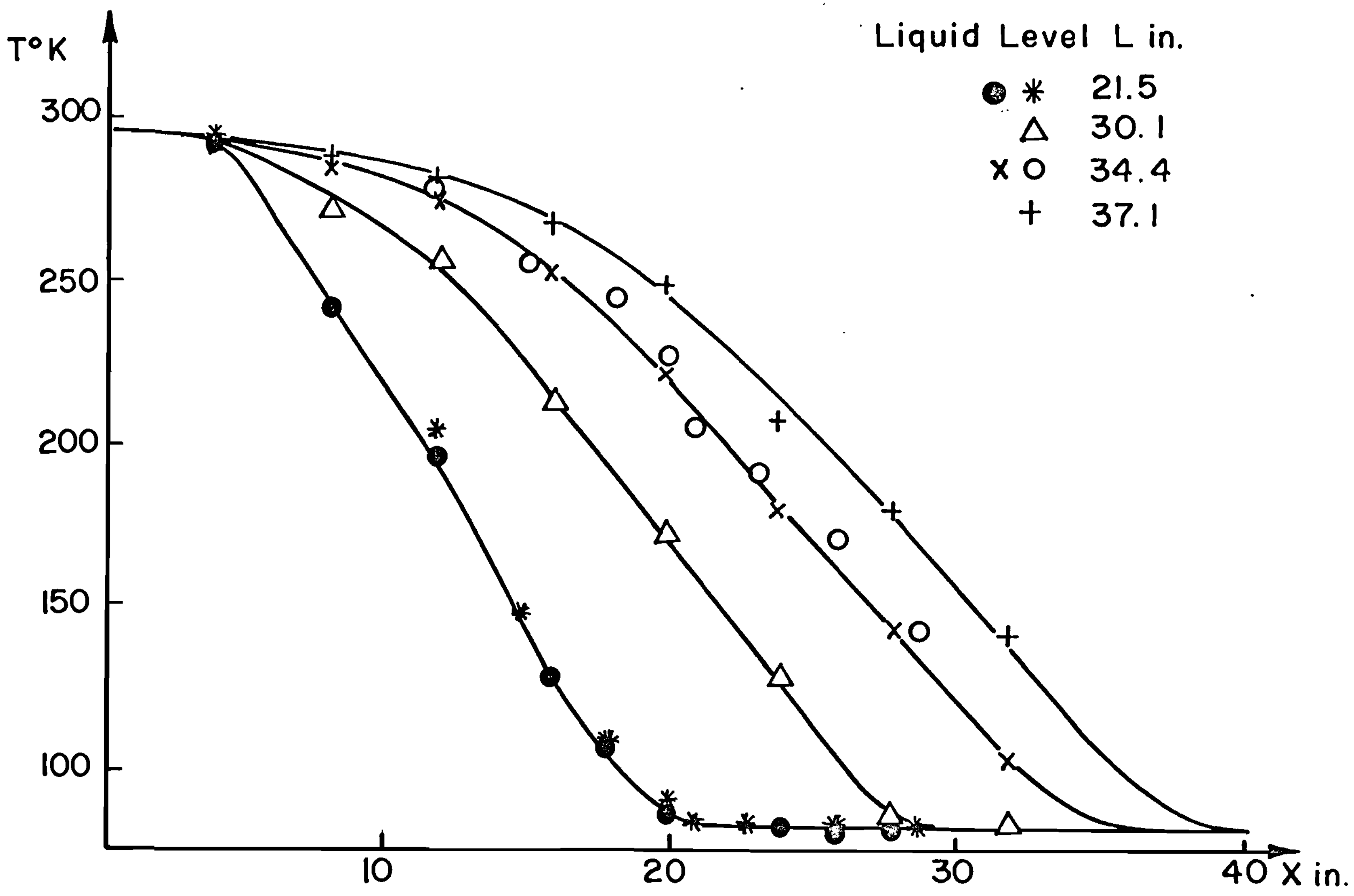

FIG. 10 TYPICAL GRADIENTS(LN$_2$COOLANT)

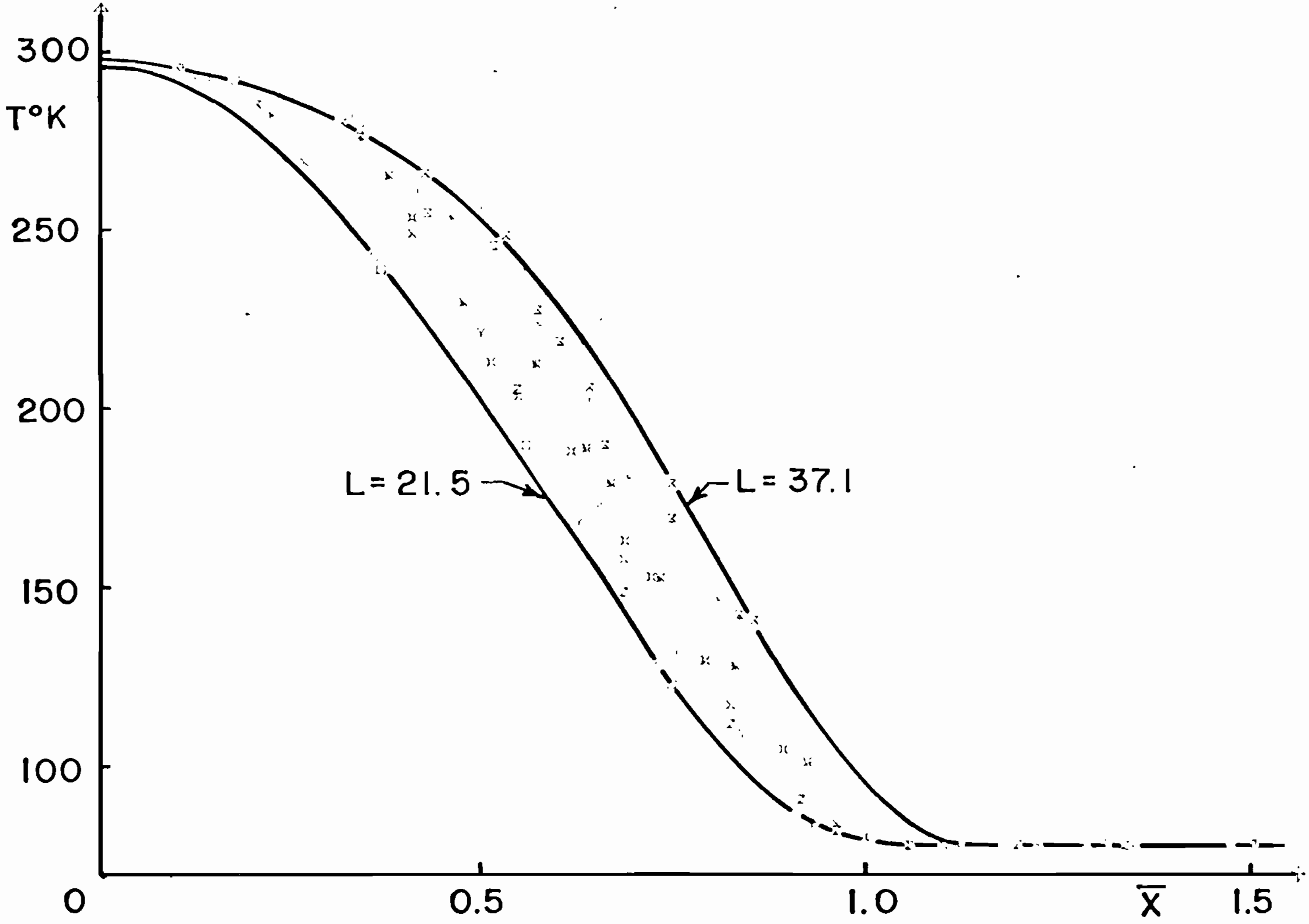

FIG. 11 GRADIENT DATA VS. $\overline{X} = X/L$ (LN_2 COOLANT)

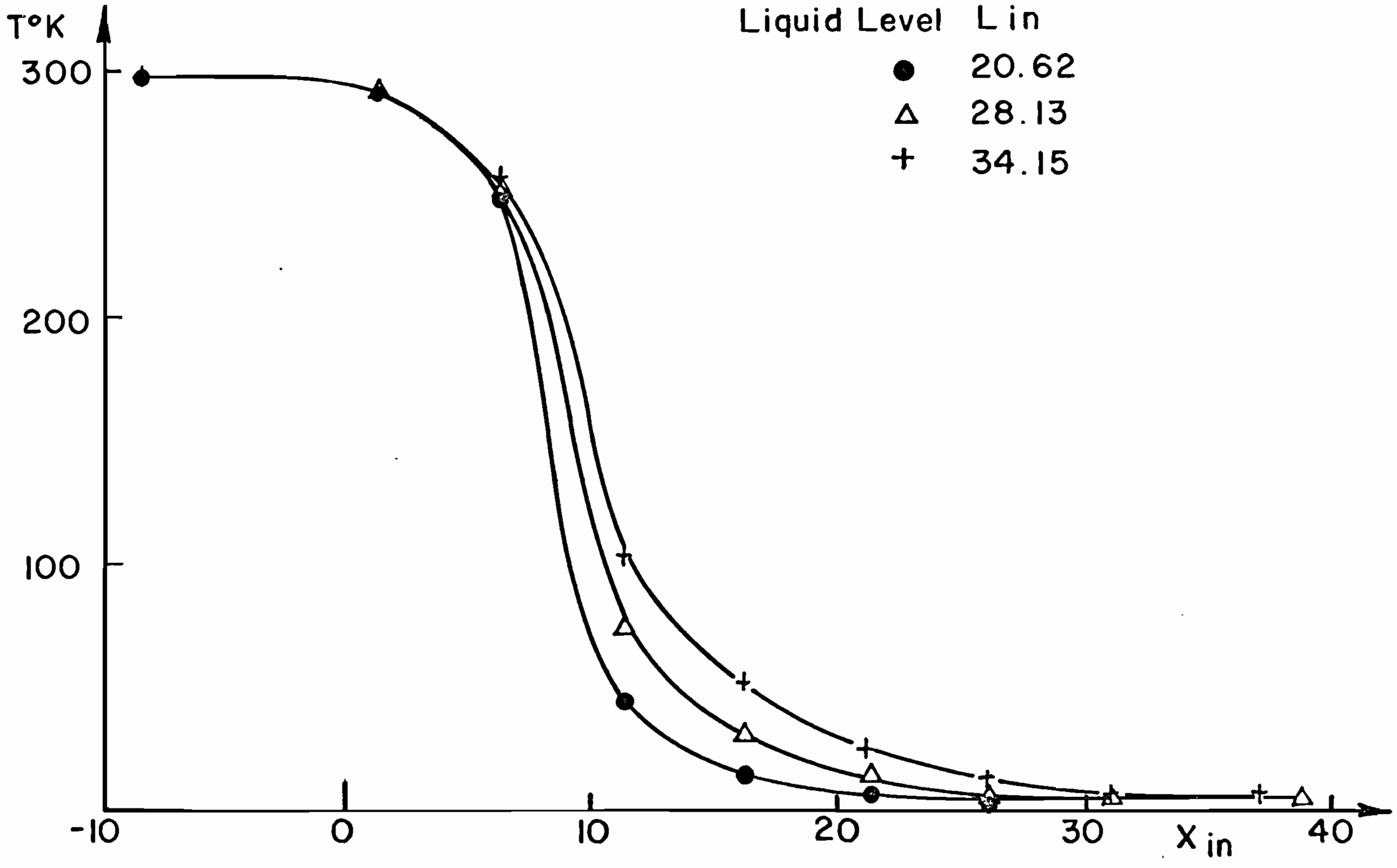

FIG. 12 TYPICAL GRADIENTS (LHe COOLANT)

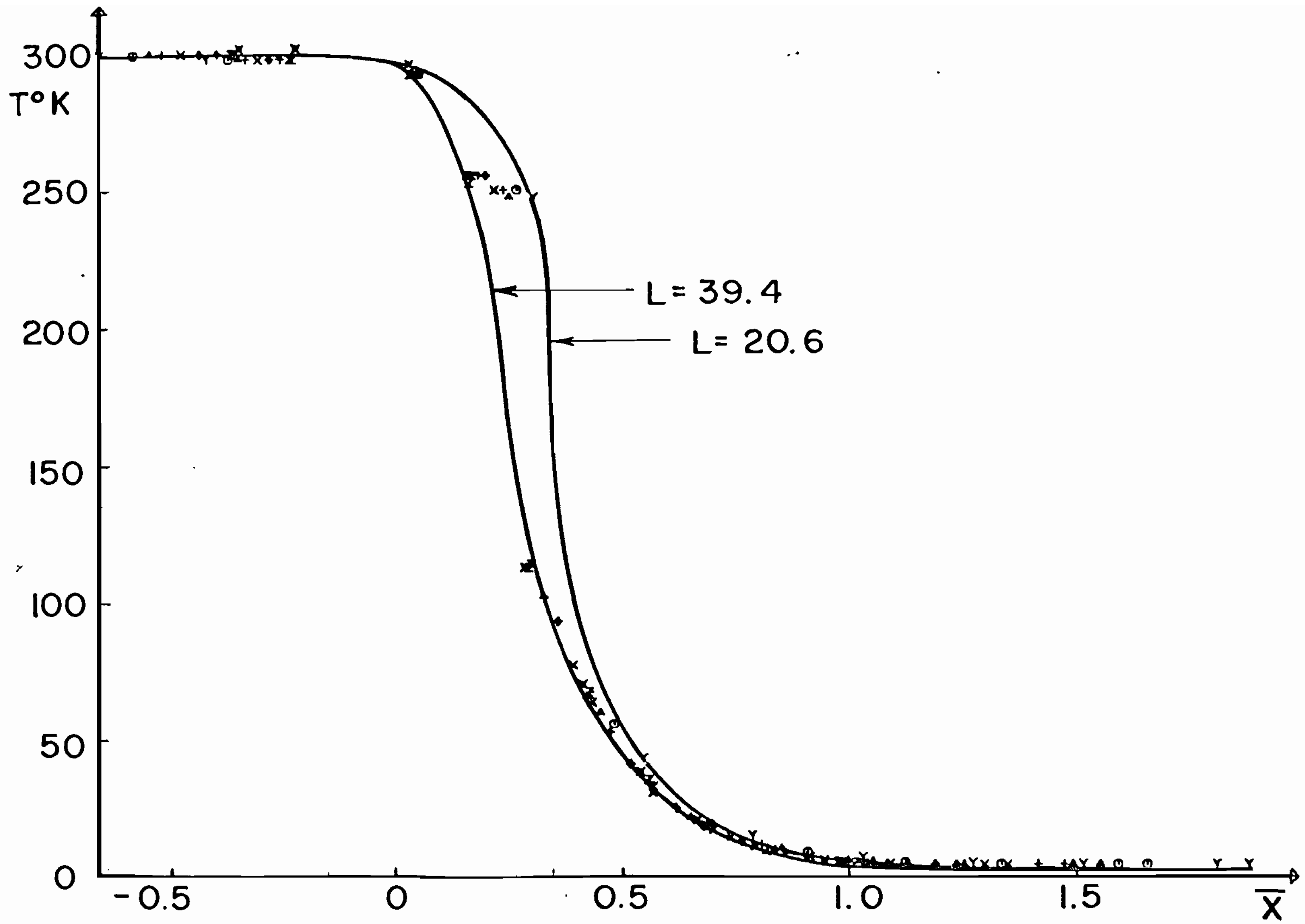

FIG. 13 GRADIENT DATA VS. $\overline{X} = X/L$ (LHe COOLANT)

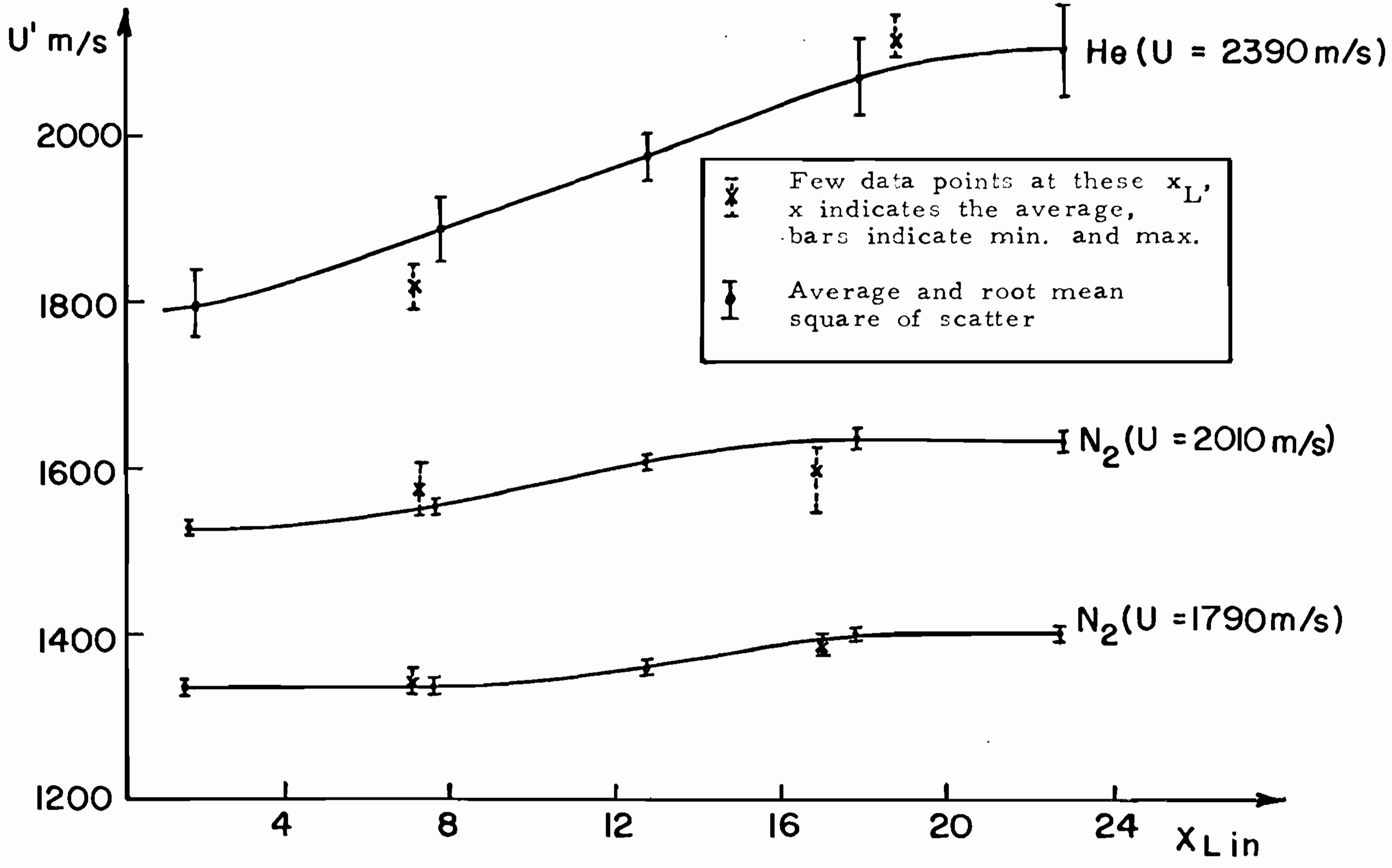

FIG. 14 MEASURED VELOCITIES (LN_2 COOLANT)

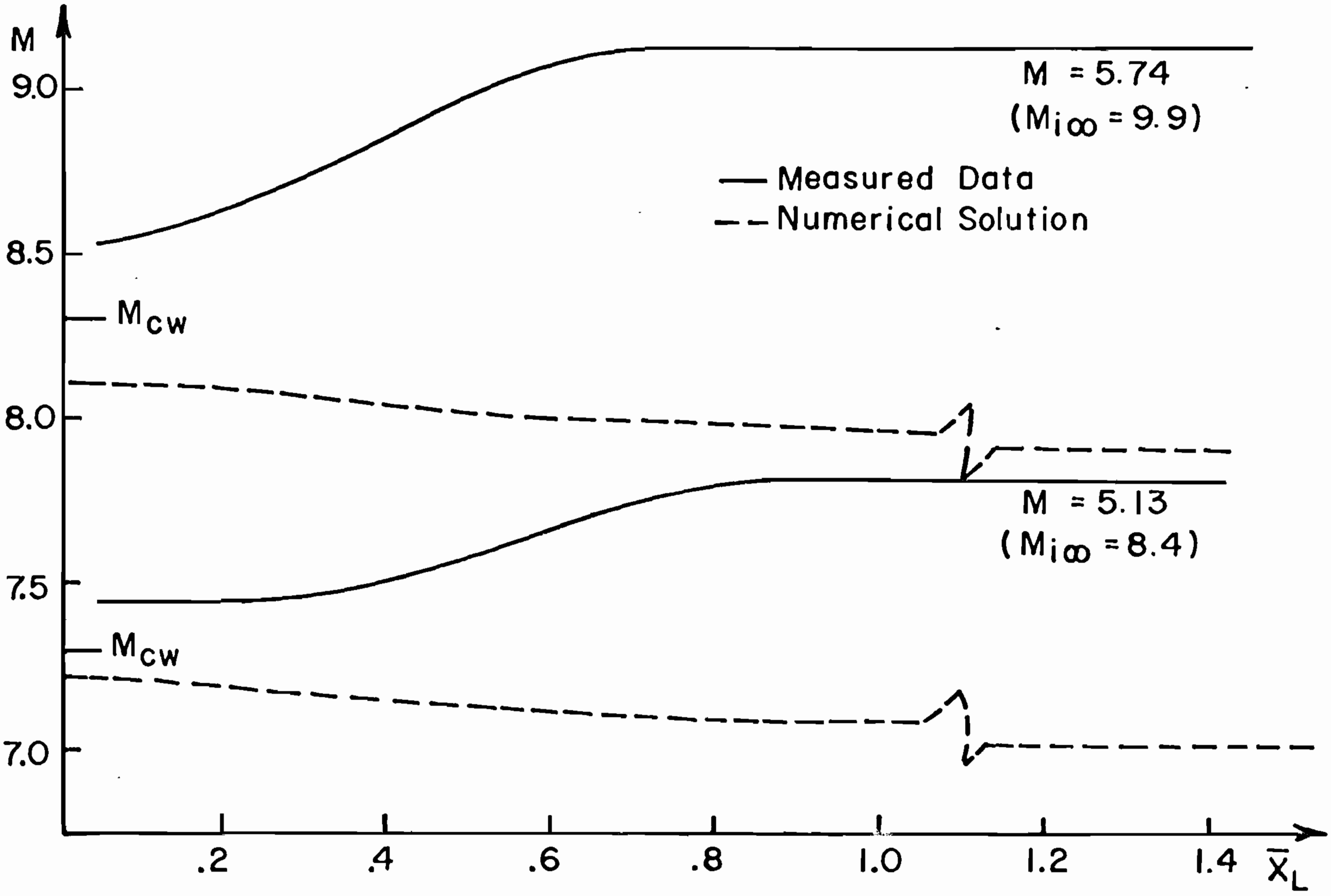

FIG. 15 $M'(\bar{X}_L)$ - TEST GAS N_2 - LN_2 COOLANT

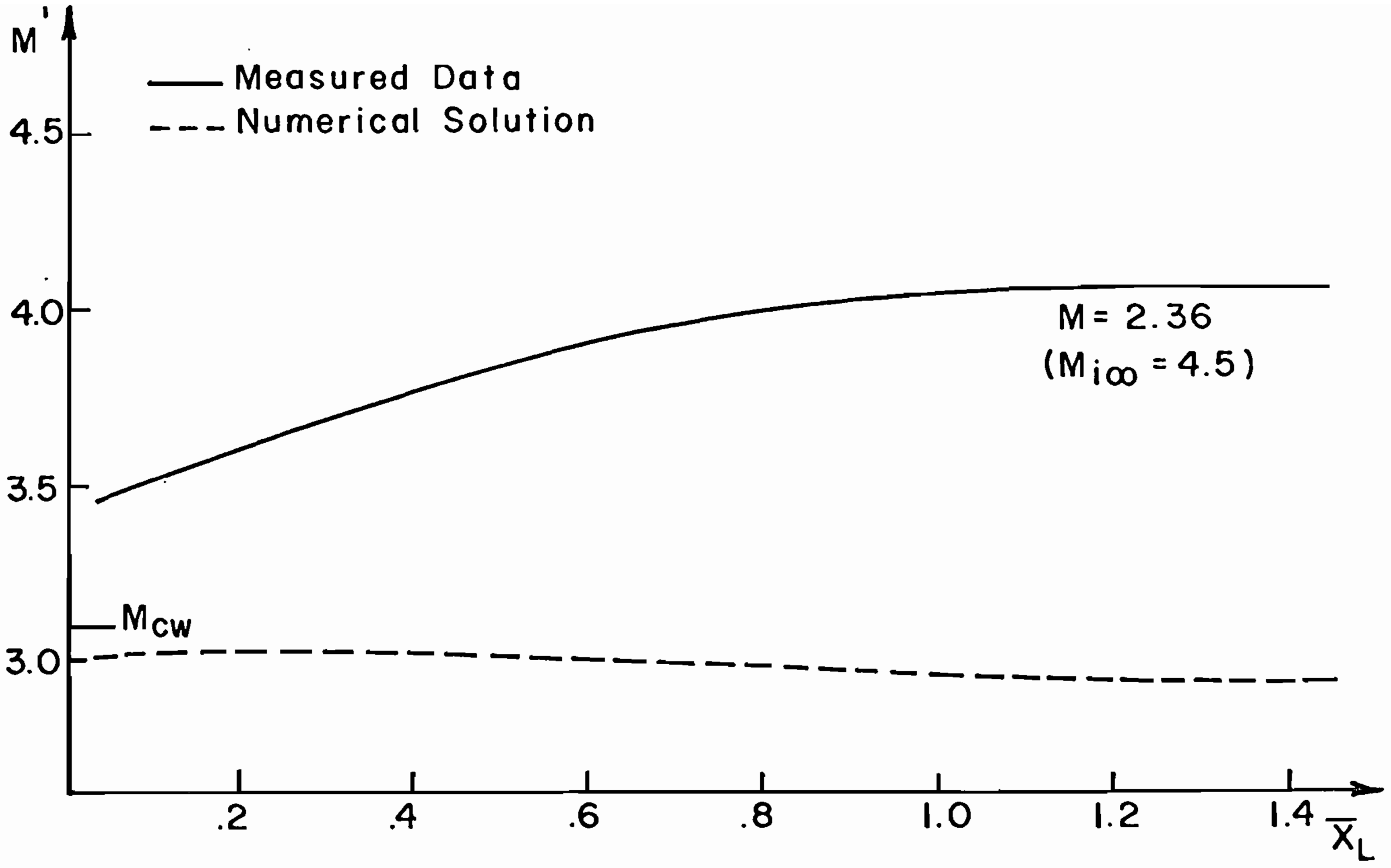

FIG. 16 $M'(\overline{X}_L)$ - TEST GAS He-LN_2 COOLANT

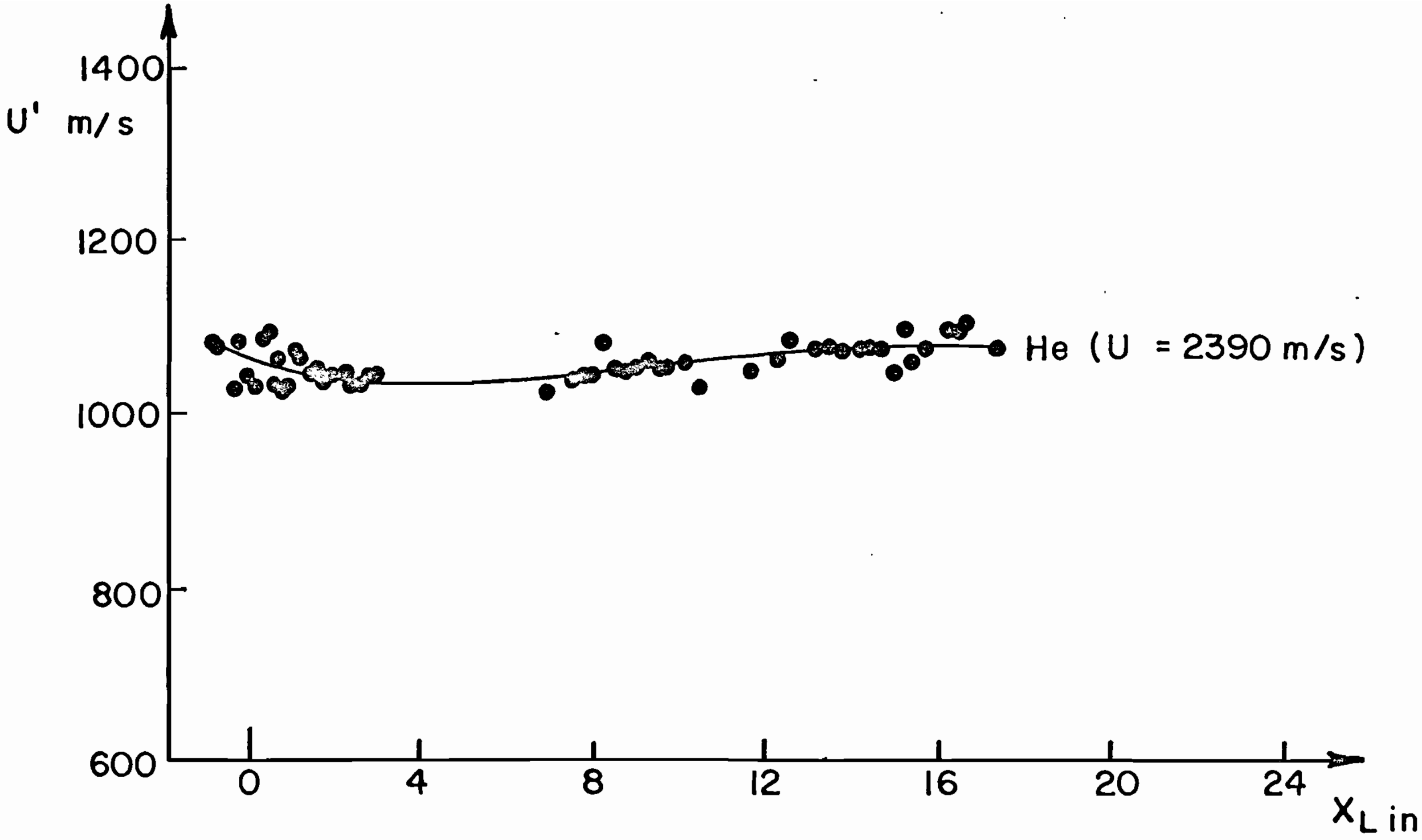

FIG. 17 MEASURED VELOCITIES (L He COOLANT)

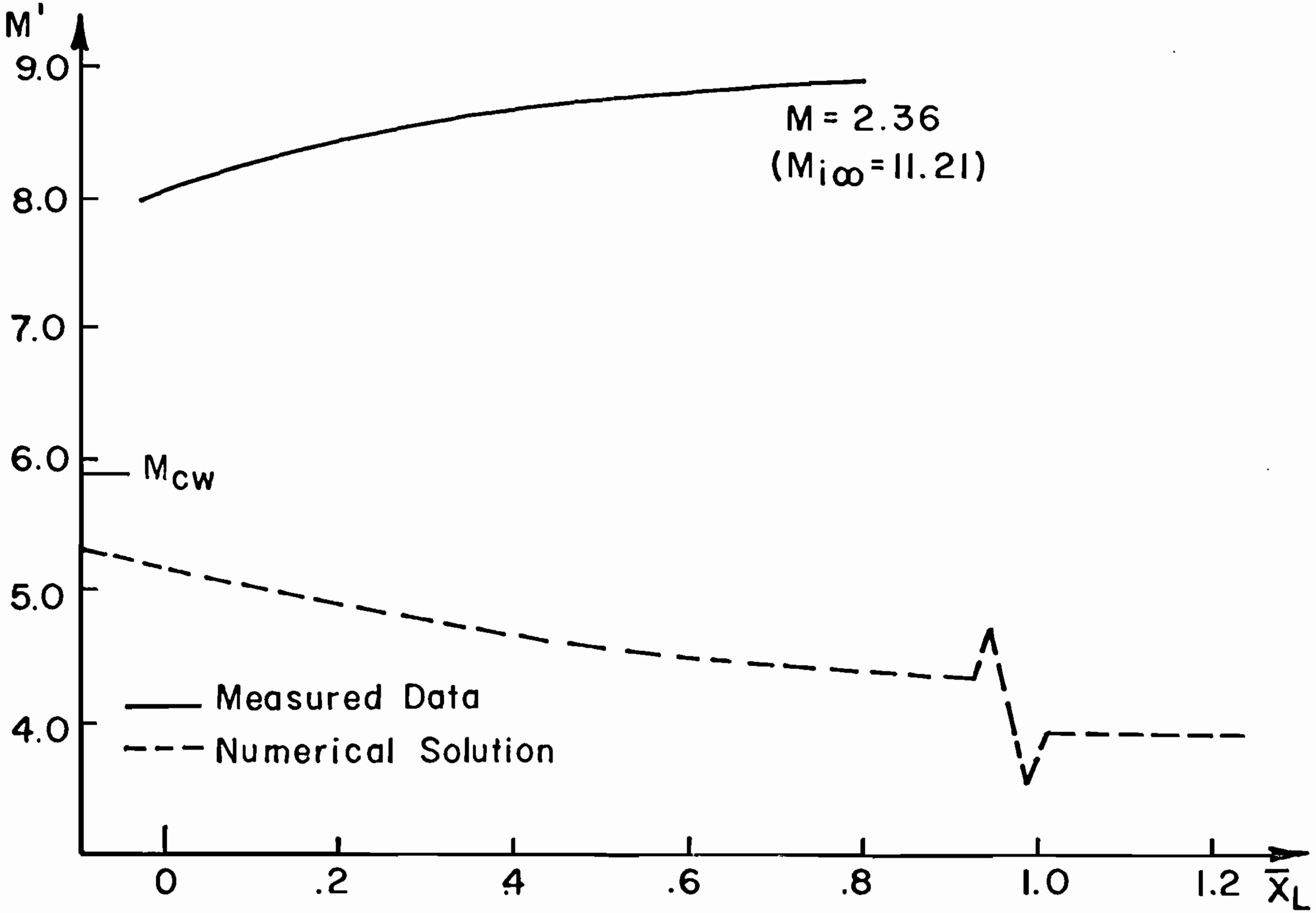

FIG. 18 $M'(\bar{X}_L)$ - TEST GAS HELIUM - LHE COOLANT

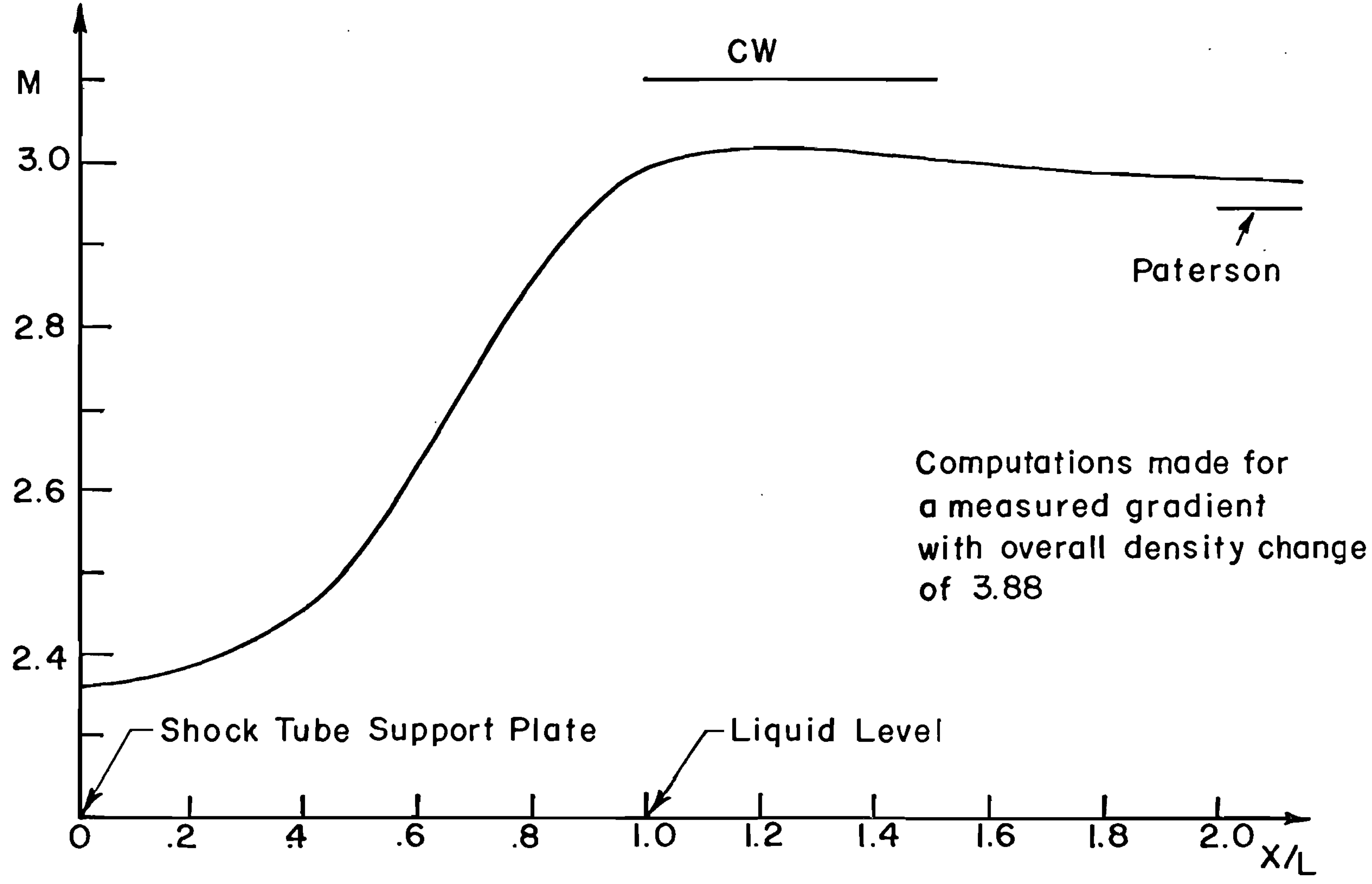

Computations made for a measured gradient with overall density change of 3.88

FIG. 19 SHOCK STRENGTHENING DUE TO A DENSITY GRADIENT ALONE

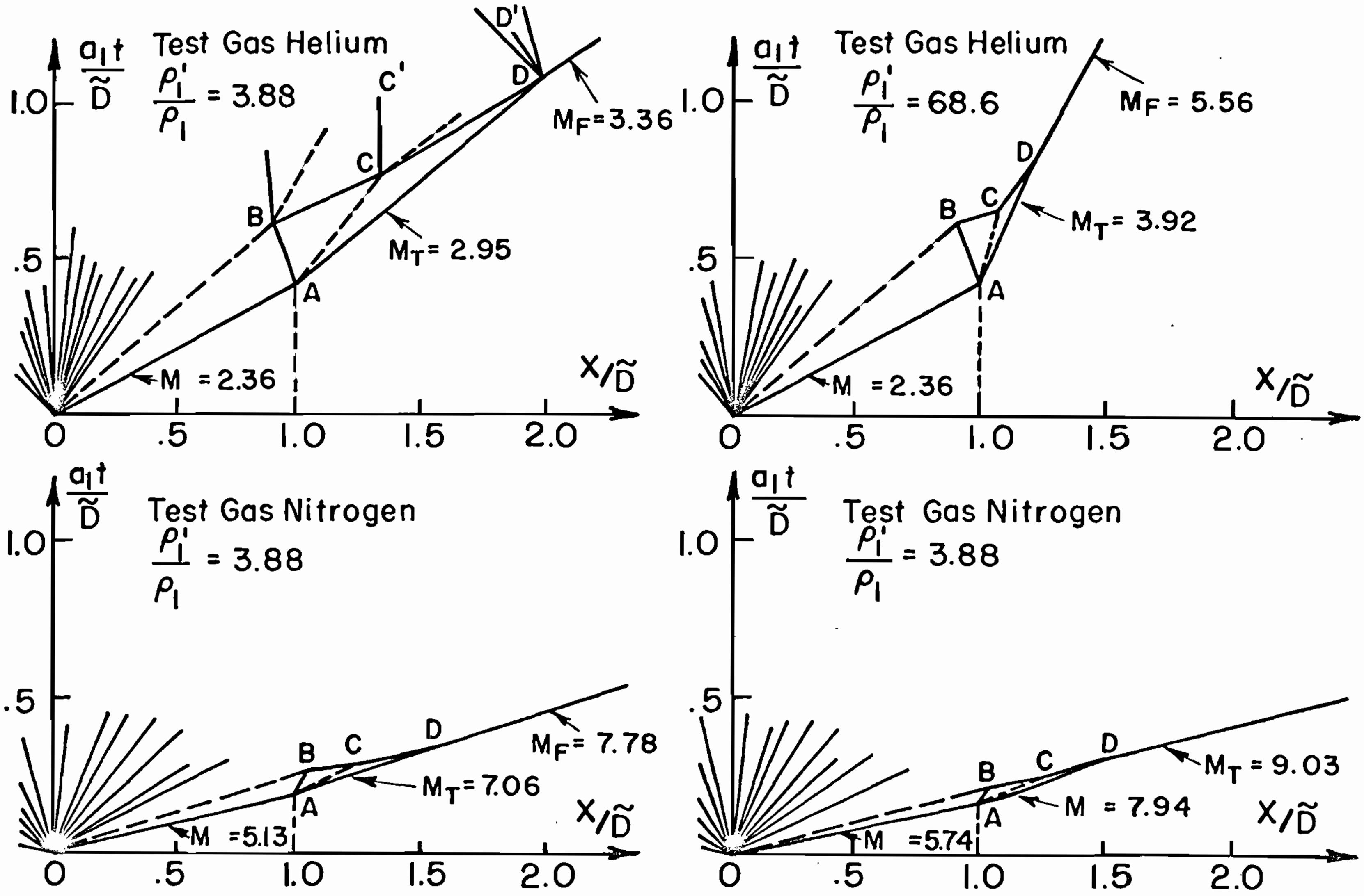

FIG. 20 WAVE PATTERN IN A SHOCK TUBE WITH A DENSITY DISCONTINUITY AT $X = \tilde{D}$ ($X = 0$ IS AT THE DIAPHRAGM)

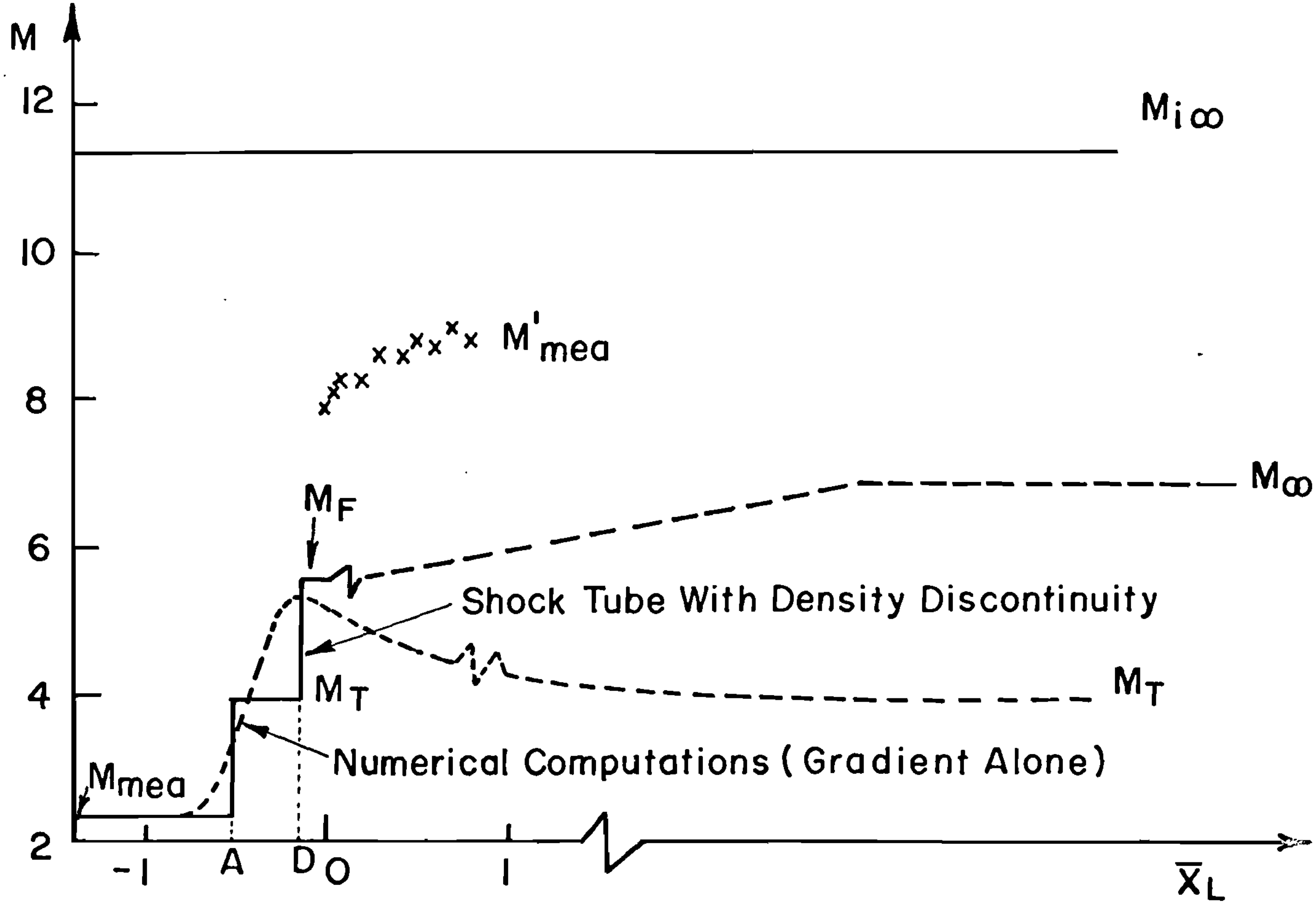

FIG. 21 a SUMMARY - TEST GAS HELIUM - LHE COOLANT

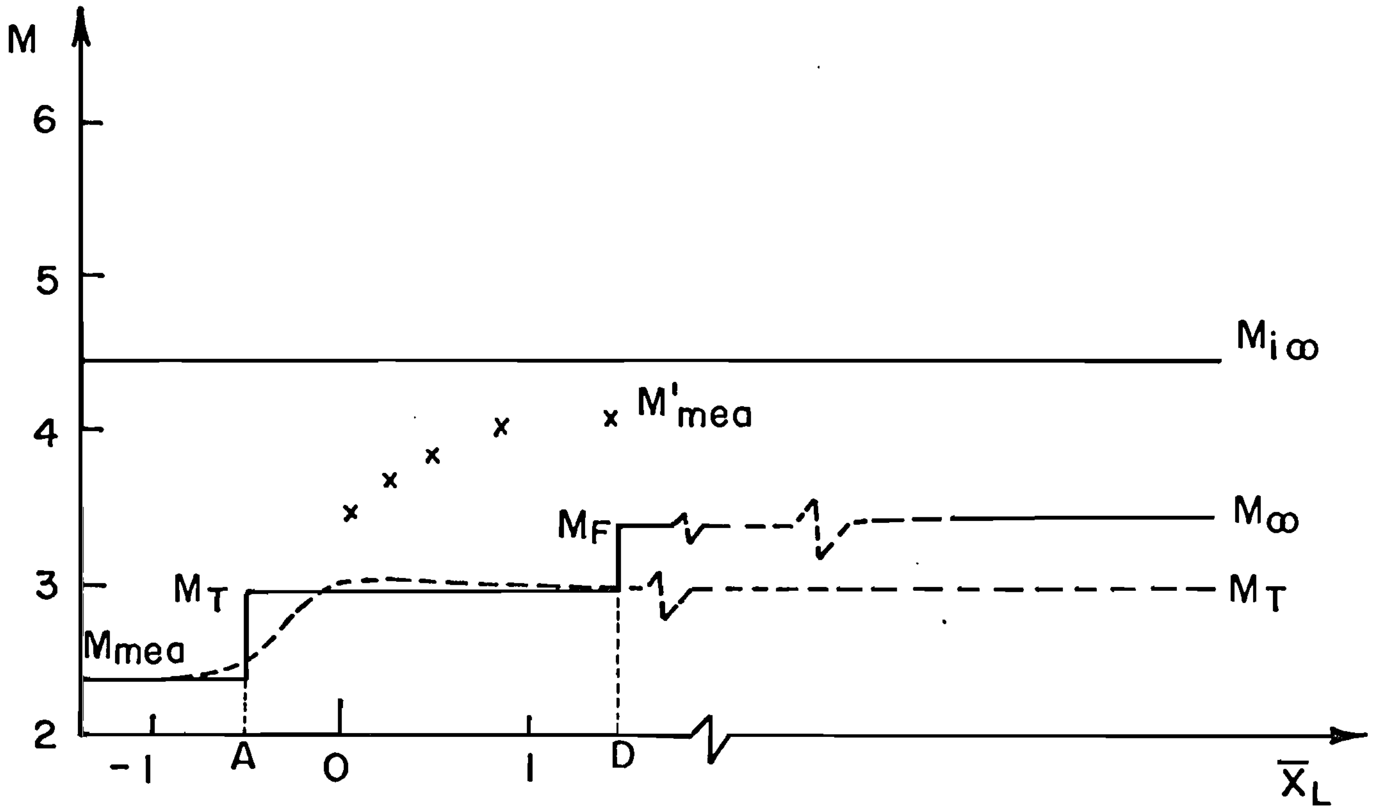

FIG. 21 b SUMMARY – TEST GAS HELIUM - LN_2 COOLANT

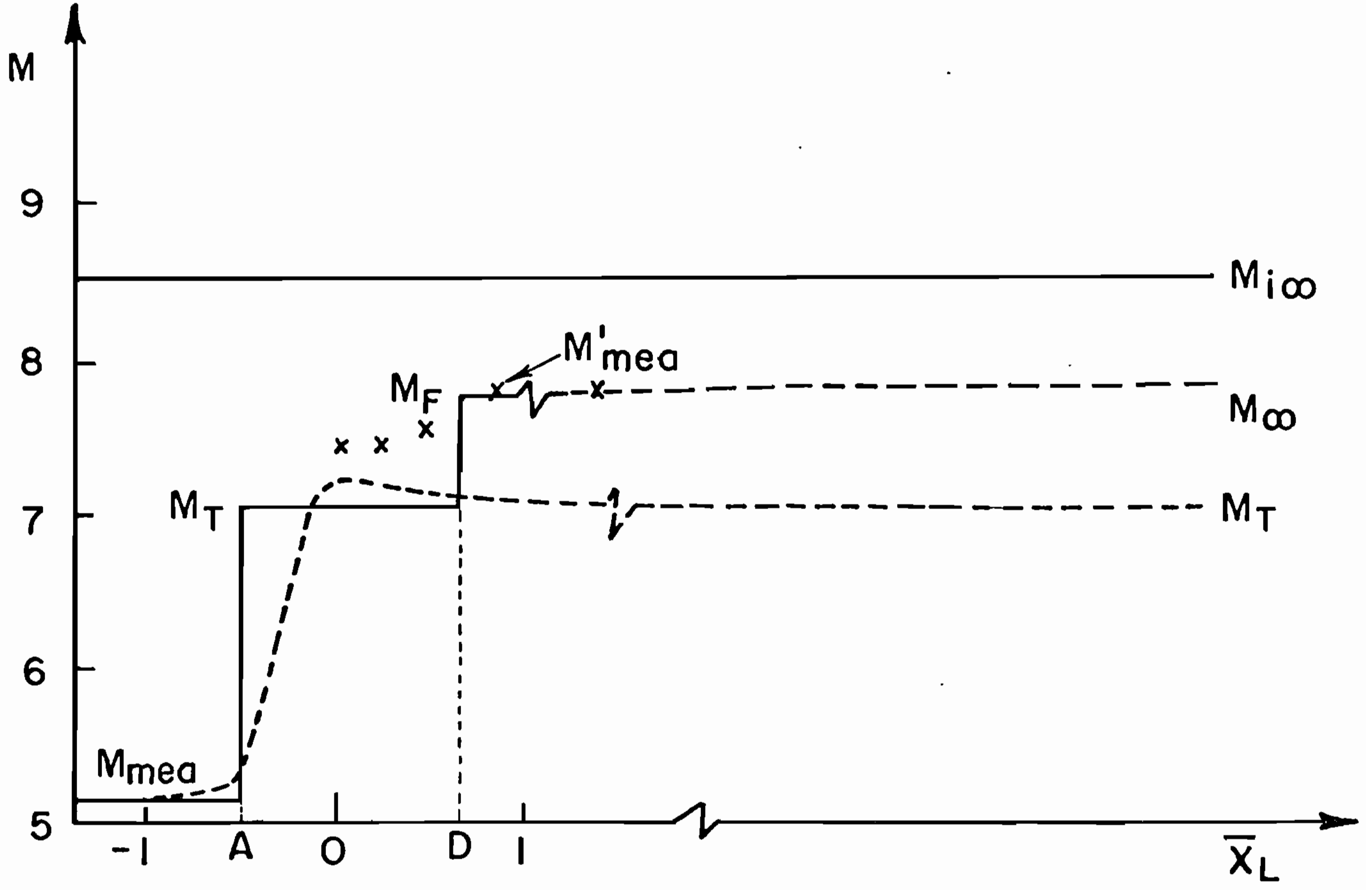

FIG. 21 c SUMMARY - TEST GAS NITROGEN - LN_2 COOLANT

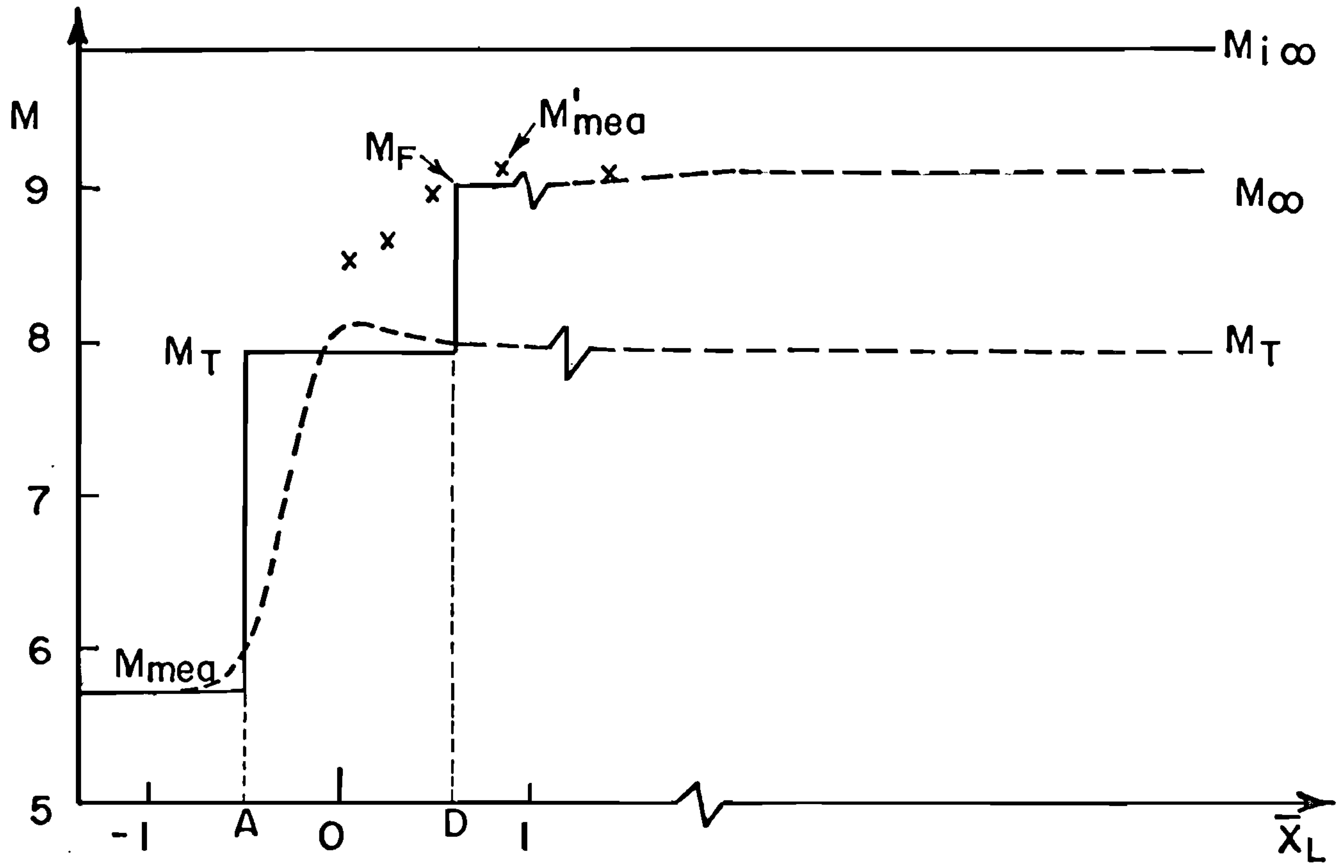

FIG. 21 d SUMMARY - TEST GAS NITROGEN - LN$_2$ COOLANT

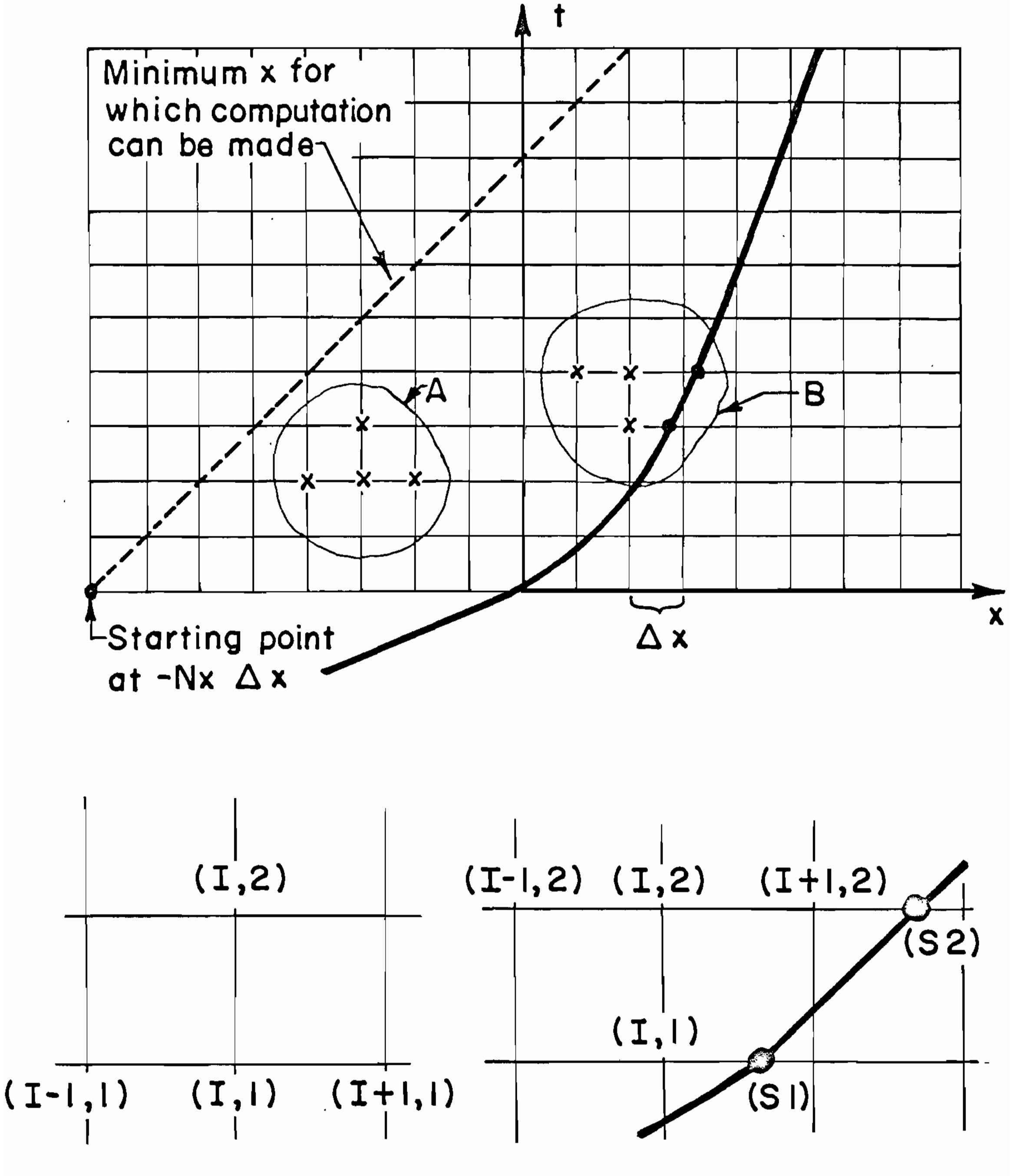

Pattern A

Pattern B

FIG. 22a NUMERICAL INTEGRATION PATTERN

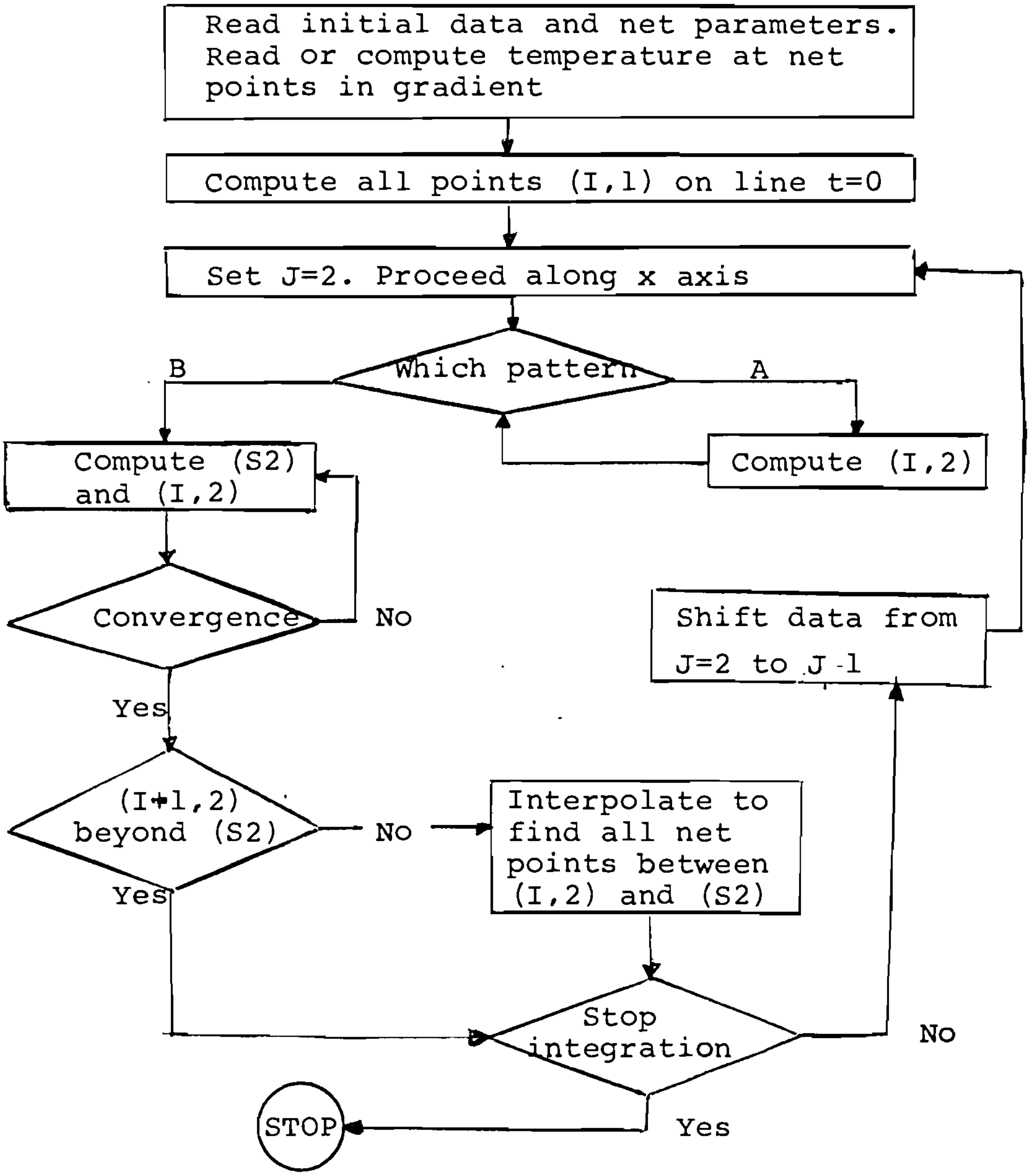

FIG. 22 b NUMERICAL INTEGRATION - COMPUTATIONS PROCEDURE

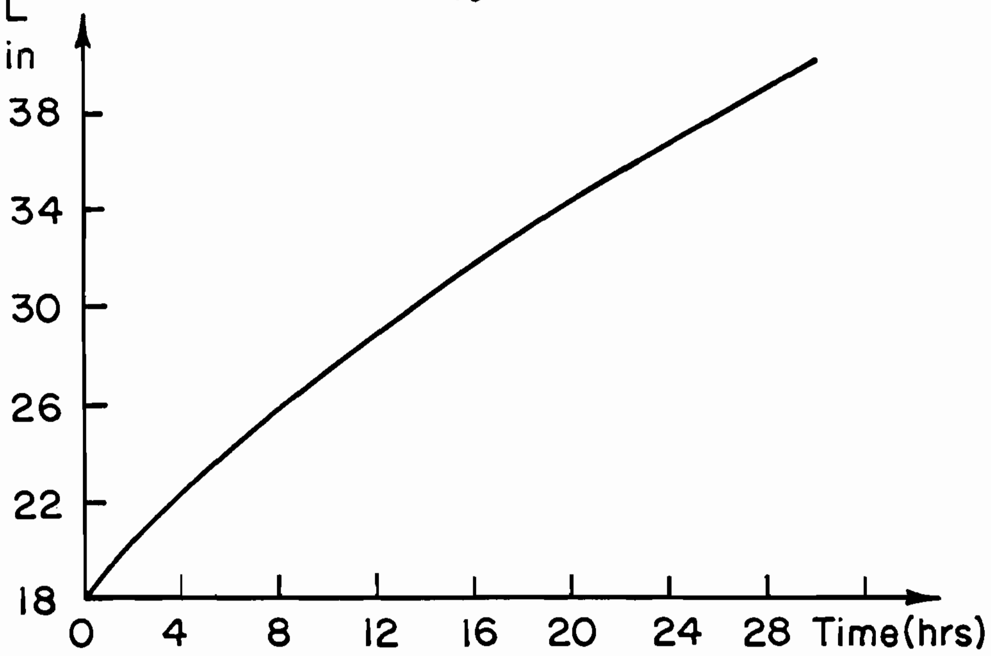

FIG.23a BOIL OFF RATE IN LN_2 DEWAR

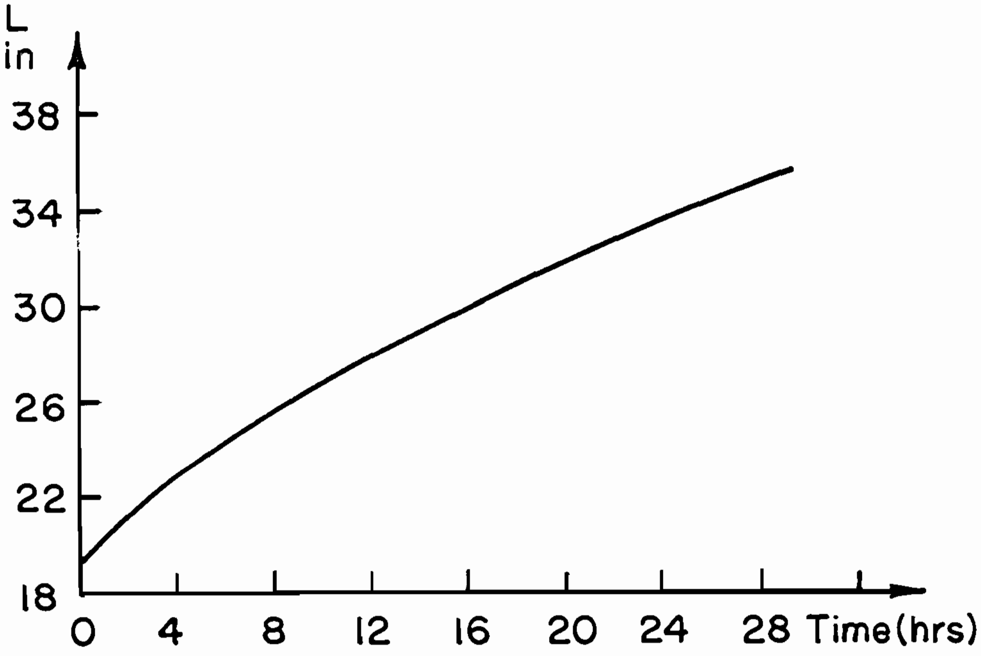

FIG. 23b BOIL OFF RATE IN LHe DEWAR

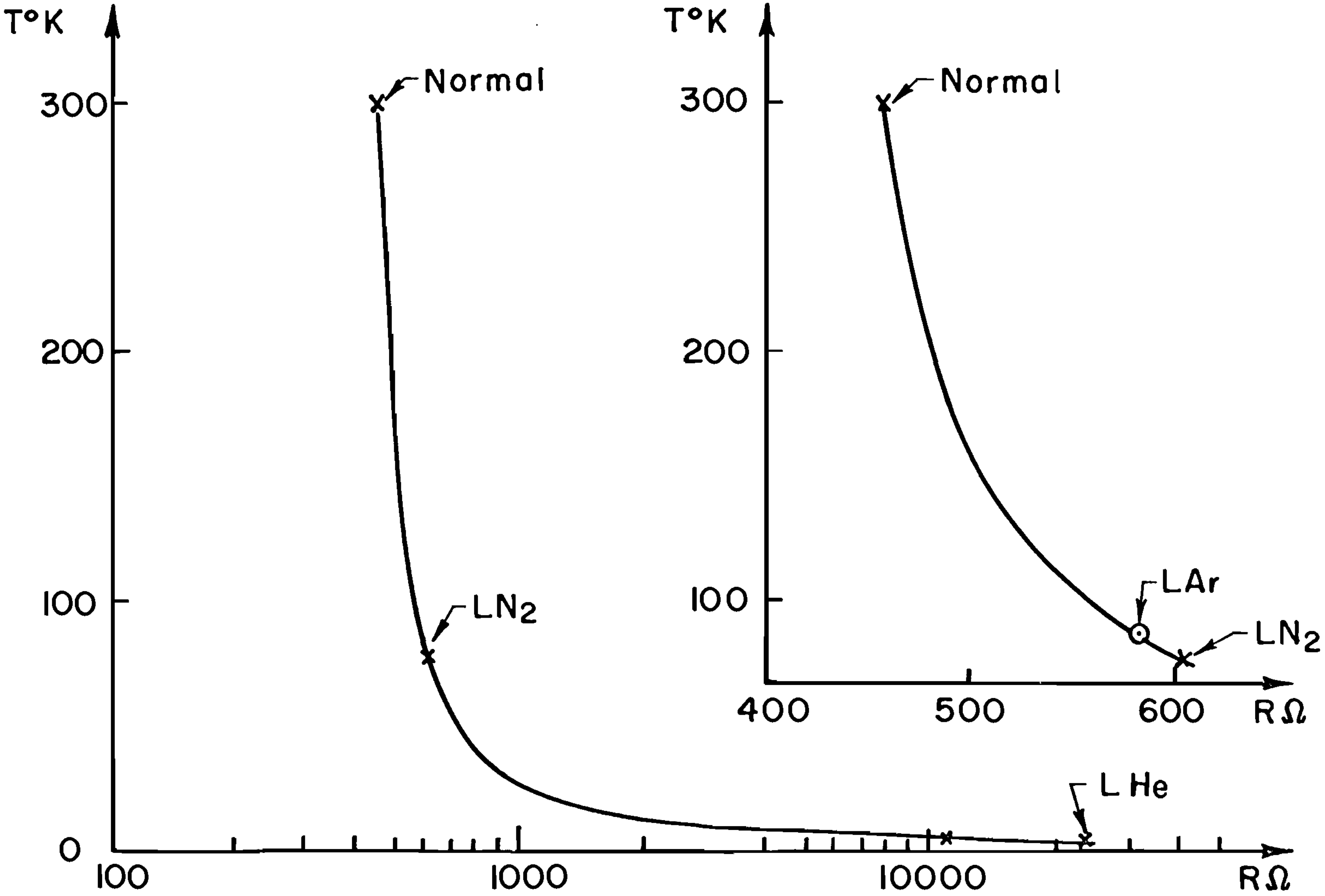

FIG. 24 TYPICAL RESISTOR CALIBRATION